

Allosteric Competition and Inhibition in AMPA Receptors

W. Dylan Hale^{1,2}, Alejandra Montaña Romero^{1,2§}, Cuauhtemoc U. Gonzalez^{3,4§}, Vasanthi Jayaraman³, Albert Y. Lau^{2*}, Richard L. Huganir^{1,5*}, & Edward C. Twomey^{1,2,6,7*}

¹Solomon H. Snyder Department of Neuroscience, Johns Hopkins University School of Medicine, Baltimore, MD USA

²Department of Biophysics and Biophysical Chemistry, Johns Hopkins University School of Medicine, Baltimore, MD USA

³Center for Membrane Biology, Department of Biochemistry and Molecular Biology, University of Texas Health Science Center at Houston, TX, USA

⁴The University of Texas MD Anderson Cancer Center UTHealth Houston Graduate School of Biomedical Sciences, The University of Texas Health Science Center at Houston, Houston, TX, USA

⁵Kavli Neuroscience Discovery Institute, Johns Hopkins University School of Medicine, Baltimore, MD USA

⁶The Beckman Center for Cryo-EM at Johns Hopkins, Johns Hopkins University School of Medicine, Baltimore, MD USA

⁷Diana Helis Henry Medical Research Foundation, New Orleans, LA USA

§Equal Contribution

*Correspondence: Twomey@jhmi.edu (ECT); rhuganir@jhmi.edu (RLH); alau@jhmi.edu (A.Y.L.)

Abstract

Excitatory neurotransmission is principally mediated by AMPA-subtype ionotropic glutamate receptors (AMPA receptors). Dysregulation of AMPARs is the cause of many neurological disorders and how therapeutic candidates such as negative allosteric modulators inhibit AMPARs is unclear. Here, we show that non-competitive inhibition desensitizes AMPARs to activation and prevents positive allosteric modulation. We dissected the noncompetitive inhibition mechanism of action by capturing AMPARs bound to glutamate and the prototypical negative allosteric modulator, GYKI-52466, with cryo-electron microscopy. Noncompetitive inhibition by GYKI-52466, which binds in the transmembrane collar region surrounding the ion channel, negatively modulates AMPARs by decoupling glutamate binding in the ligand binding domain from the ion channel. Furthermore, during allosteric competition between negative and positive modulators, negative allosteric modulation by GYKI-52466 outcompetes positive allosteric modulators to control AMPAR function. Our data provide a new framework for understanding allostery of AMPARs and foundations for rational design of therapeutics targeting AMPARs in neurological diseases.

Introduction

The human brain consists of roughly 100 billion neurons¹. Central to the brain's function is the ability of neurons to communicate with one another². Most of the communication between neurons occurs at contact sites called synapses. There are over 100 trillion synaptic connections between neurons in the brain, and most of these synapses are glutamatergic, where the neurotransmitter glutamate (Glu) is released by a pre-synaptic neuron and received by a post-synaptic neuron³. Ionotropic glutamate receptors (iGluRs) in the membrane of the post-synaptic neuron bind Glu and allow positively charged ions to enter the post-synaptic neuron, which depolarizes the post-

1 synaptic membrane⁴. This excites a signaling cascade in the post-synaptic neuron that enables
2 signaling to be transduced to other neurons and is vital for information processing. Specialized
3 iGluRs, α -amino-3-hydroxy-5-methyl-4-isoxazolepropionic acid receptors (AMPA), initiate the
4 depolarization of the post-synaptic neuron and contribute to the activation of the other iGluR
5 subtypes². AMPARs mediate the majority of fast, synchronous excitation in the vertebrate brain
6 and proper signaling of AMPARs in the post-synaptic membrane is required for healthy brain
7 function.

8
9 Dysregulation of AMPARs is a major contributor to many neurological disorders. These include
10 schizophrenia, anxiety, chronic pain, epilepsy, learning impairment, Alzheimer's, and
11 Parkinson's⁴. A principal approach to therapeutically targeting AMPARs is through allosteric
12 modulation with small molecules. Allosteric modulators enable AMPAR function to be positively
13 or negatively tuned from binding sites independent of Glu binding. Such molecules are clinically
14 promising with broad applications across neurological disorders. However, despite the central
15 role of AMPARs in synaptic signaling and their roles in human diseases, only a single molecule,
16 perampanel (Fycompa®), is approved by the US FDA for targeting AMPARs for therapeutic
17 benefit^{4,5}. Perampanel is approved by the FDA to treat epilepsy⁶, and perampanel/perampanel-
18 like molecules (PPLMs) also show promise in treating chronic pain. PPLMs belong to a class of
19 noncompetitive inhibitors typified by the prototype compound 4-(8-Methyl-9H-1,3-dioxolo[4,5-
20 h][2,3]benzodiazepin-5-yl)-benzenamine dihydrochloride (GYKI-52466)^{4,7,8}, which binds to the
21 AMPAR transmembrane domain (TMD)⁹. PPLMs exert characteristically similar effects on
22 AMPAR function and bind to the same site in the TMD^{5,8-11}. In the presence of PPLMs, AMPARs
23 show a marked reduction in ion channel conductance irrespective of agonist concentration, and
24 PPLMs inhibit channel function irrespective of channel state or membrane voltage^{5,8-11}. PPLMs
25 are effective at reducing epileptic behavior in mice and *in vitro*^{12,13}, but perampanel treatment in
26 humans produces undesirable side effects such as dizziness, somnolence, and ataxia¹⁴,
27 underscoring the need for refined AMPAR inhibitors for treating neurological disorders. While the
28 binding sites of PPLMs have been generally described⁹, the mechanism by which PPLMs inhibit
29 AMPAR function is unknown. This is a major roadblock in therapeutically targeting AMPARs with
30 improved inhibitors.

31
32 AMPARs are tetrameric ligand-gated ion channels, made up of GluA1-4 subunits, encoded by the
33 *Gria1-4* genes⁴. AMPARs couple extracellular binding of Glu to ion flux across the postsynaptic
34 membrane by physically linking four extracellular clamshell-shaped ligand binding domains
35 (LBDs) to transmembrane (TM) helices that occlude entry to the cation channel (**Fig. 1a**)^{15,16}. Glu
36 binding to the AMPAR LBDs initiates the gating cycle in which the receptors transition through
37 their main functional states: resting, activated, and desensitized^{4,17}. Activation begins with Glu
38 binding, which drives the lower half of the LBD clamshell (D2) closer to the upper half (D1) of the
39 LBD, closing the LBD clamshell-like structure around the neurotransmitter (**Fig. 1a**)^{15,16}. AMPAR
40 LBDs locally dimerize within the tetrameric receptor, and coordinated clamshell closure
41 maximizes the interface between the upper D1 lobes of LBD dimer pairs (**Fig. 1a**). Movement of
42 the D2 LBD lobes following Glu binding activates the receptor by pulling open the M3 TM helices
43 that define the receptor pore along with the M2 helices, which define the selectivity filter, enabling
44 cation influx. However, the active state is short-lived, and the receptor quickly desensitizes
45 following activation to protect the neuron from toxic influx of cations. Desensitization occurs when
46 the LBDs roll away from each other, which ruptures the D1 interface and closes the ion channel
47 below and reduces separation between the LBD D2's. AMPARs return to their resting state after
48 unbinding Glu (**Fig. 1a**)¹⁸.

49
50 Allosteric modulators bind to AMPARs at sites distinct from the Glu binding site in the LBD and
51 bias AMPAR function. Positive allosteric modulators such as cyclothiazide (CTZ) and its

1 derivatives bind between the D1's of local LBD dimers and enhance D1-D1 contact during
2 activation, thus favoring activation and preventing AMPAR desensitization¹⁹⁻²². How negative
3 allosteric modulators such as PPLMs prevent AMPAR activation is more enigmatic. The current
4 paradigm in the field is that PPLMs bind to the region of the TMD that is extracellular facing and
5 prevent AMPARs from transitioning to the active state^{4,9}. How this occurs is unknown because
6 AMPARs have not been studied structurally in the presence of both Glu and PPLMs^{9,23}. Thus,
7 while these studies describe binding sites, the mechanism of inhibition is unclear because the
8 PPLMs are bound to resting state receptors.

9
10 We hypothesized that PPLMs allosterically inhibit AMPARs by pushing the receptors into a
11 desensitized-like state that decouples Glu binding from the ion channel. Furthermore, we
12 expected there to be allosteric competition between positive modulators such as CTZ and
13 negative modulators such as PPLMs to control AMPAR function because their binding sites in
14 AMPARs are at distinct sites. How this would occur is unknown and not yet observed in AMPARs
15 nor any family of ligand gated ion channels.

16
17 To test these ideas, we activated AMPARs in the presence of both the negative allosteric
18 modulator GYKI-52466 and positive allosteric modulator CTZ. Through a combination of cryo-
19 electron microscopy (cryo-EM), single-molecule fluorescence resonance energy transfer
20 (smFRET), electrophysiology, and molecular dynamics simulations, we demonstrate that GYKI-
21 52466 binding in the TMD decouples Glu binding from the ion channel by allosterically rearranging
22 the AMPAR LBD. In addition, GYKI-52466 binding in the TMD prevents positive allosteric
23 modulation by CTZ in the LBD. Our findings shed new insights into how allosteric modulation is
24 coordinated across AMPARs, demonstrate allosteric competition between modulators, and will
25 invigorate structure-based drug design against AMPARs and provide a framework for studying
26 inhibition across iGluRs and other ligand-gated ion channels.

27 28 **Results**

29 30 *Structures of inhibited AMPAR complexes*

31
32 To identify how PPLMs inhibit AMPARs via negative allosteric modulation and test our idea of
33 allosteric competition, we purified homotetrameric AMPARs composed of the GluA2 subunit in
34 complex with the auxiliary subunit transmembrane AMPAR regulator protein (TARP) γ 2^{15,18,24},
35 which enhances AMPAR activation (**Extended Data Fig. 1a,b**), and preincubated the receptors
36 with cyclothiazide (CTZ), a positive allosteric modulator that inhibits AMPAR desensitization and
37 allows the activated state of the receptor to be captured with cryo-EM^{15,25}. We activated these
38 AMPAR complexes in the presence of GYKI-52466 to capture inhibited states (**Extended Data**
39 **Fig. 1c**). We captured inhibited states through two different schemes. In the first scheme (inhibited
40 state 1, IS-1), we mixed the CTZ-bound receptors with Glu and GYKI-52466 immediately prior to
41 freezing. In the second scheme (IS-2), the receptors were pre-incubated with GYKI-52466 in
42 addition to CTZ, and Glu was added immediately before freezing. Each approach resulted in
43 similar inhibited states (**Extended Data Fig. 2a**).

44
45 We focus our analysis on IS-1 owing to higher data quality (**Extended Data Figs. 3,4**). The overall
46 structure of the AMPAR complexes reveal key details of an inhibited AMPAR (**Fig. 1b**). There is
47 an overall "Y" arrangement of the receptor, with the two-layered ECD comprised of the ATD and
48 LBD. All four GluA2 LBDs are Glu-bound. Immediately below is the GluA2 TMD, which is fully
49 occupied with four TARP γ 2 auxiliary subunits. Four GYKI-52466 molecules are bound to the TMD
50 along its extracellular-facing surface.

51

1 Cryo-EM reconstruction of the AMPAR TMD to 2.6 Å enables elucidation of key features of the
2 AMPAR TMD during inhibition. The four GYKI-52466 molecules are wedged between helices at
3 the top of the TMD (**Fig. 1c**). Importantly, the GYKI-52466 binding sites are adjacent to the ion
4 channel in the channel collar region. The collar channel forms a ring of solvent accessible pockets
5 for PPLMs that surrounds the M3 gate. Lipids adorn the AMPAR TMD on both the extracellular
6 and cytosolic facing (**Fig. 1c**) and are critical to plug cavities within the bilayer that would otherwise
7 perturb the solvent accessibility of the ion channel (**Extended Data Fig. 5**). Next, we measured
8 the ion channel radius, which indicates a closed channel; the upper channel gate, defined by
9 M629 at the M3 helix crossing, completely restricts channel access (< 1.0 Å radius) to both water
10 molecules and sodium ions (**Fig. 1d**).

11
12 While both activator (Glu) and negative allosteric modulator (GYKI-52466) are bound to the
13 AMPAR, the positive allosteric modulator CTZ, which was included in the preparation of both IS-
14 1 and IS-2, is absent from both cryo-EM reconstructions. This indicates that the states we
15 captured are markedly different from previously captured states of AMPARs, as CTZ binds to both
16 the resting and activated states of the receptor²⁵⁻²⁷. Thus, GYKI-52466, at a binding site
17 completely distinct from that of CTZ in the AMPAR LBD allosterically outcompetes CTZ.

18
19 *The GYKI-52466 binding site*

20
21 Reconstruction of the AMPAR TMD enabled precise building of the AMPAR TMD (**Extended**
22 **Data Fig. 6a**). However, to delineate the precise details of GYKI-52466 binding in the AMPAR
23 channel collar we used symmetry expansion to reconstruct the binding site to 2.2 Å resolution
24 (**Extended Data Fig. 6b-e**). This enabled us to characterize the complete binding pocket (**Fig.**
25 **2a,b**). GYKI-52466 is partially stabilized in the collar through a π -bond stack where GYKI-52466
26 is sandwiched between F623 at the top of the M3 helix and the P520 on the pre-M1 helix (**Fig.**
27 **2a**). Van der Waals forces from five nearby residues, S516, N619, S615, Y616, and N791 also
28 contribute to the binding site (**Fig. 2b**). The N3 of GYKI-52466 is sandwiched between both Y616
29 on M3 and S615 on the M3 of an adjacent subunit. Therefore, GYKI-52466 is wedged between
30 two AMPAR subunits in the TMD (**Fig. 2b**). Unique to GYKI-52466 pocket from other PPLM-
31 bound structures^{9,23} is the likely contribution of water molecules to the binding pocket (**Extended**
32 **Data Fig. 6e**) and coordination by N791 on M3 (**Fig. 2a**).

33
34 During AMPAR activation the AMPAR subunits in the B and D positions undergo the most
35 dramatic conformational changes in the TMD to drive opening of the ion channel.^{15,16,28} Because
36 of this, we hypothesized that the binding pocket around GYKI-52466 may be more compact in the
37 B/D positions during inhibition because GYKI-52466 may directly block the conformational
38 changes in the B/D positions that are associated with activation.

39
40 To assess the overall shape and size of the binding pockets in each subunit, we measured the
41 distances between P520, N791, S615 and F623 (**Fig. 2c**). To our surprise, the binding pockets
42 were remarkably similar as indicated by inter-residue distances (**Fig. 2d**). On average, there is a
43 ~12 Å distance between pairs P520-N791 as well as S615-F625, ~9 Å distance between N791-
44 S615, and ~8 Å distance between F623-P520. Thus, the shape around the GYKI-52466 binding
45 site is roughly the same in each binding pocket. The solvent accessible surface around GYKI-
46 52466 is also similar in each AMPAR subunit position, with an average solvent accessible surface
47 of ~493 Å² around GYKI-52466. Thus, despite activation being accompanied by dramatic
48 rearrangements in the B and D subunits to accommodate ion channel opening, there are no
49 discernible differences between subunit positions in the inhibited state. Thus, we expected that
50 the mechanism of allosteric inhibition by GYKI-52466 is driven through an alternative mechanism,
51 despite the GYKI-52466 binding site being within the TMD.

1
2 *GYKI-52466 Decouples Ligand Binding from Ion Channel Opening*

3
4 To elucidate the inhibition mechanism, we compared our inhibited state structure to an activated
5 state AMPAR structure (**Fig. 3a**). The majority of the TMD is largely similar between the two
6 states, except at the channel gate, which is formed by the top of the M3 helices (**Fig. 3a**). During
7 activation, the M3 helices kink outward from the pore axis to open the channel. This key
8 movement is blocked by the presence of GYKI-52466 in the B/D AMPAR subunit positions due
9 to the presence of GYKI-52466 in the channel collar (**Fig. 3a**, inset i). However, there are no key
10 differences between the GYKI-52466 B/D and A/C positions of the channel collar in the inhibited
11 state (**Fig. 2d**). In addition, each individual LBD in the inhibited state is Glu-bound, with a similar
12 overall conformation to individual LBDs in the activated state (**Fig. 3b**). We hypothesized that the
13 conformational changes that dictate AMPAR inhibition occur in the LBD layer because the ATD
14 does not play a significant role in gating²⁹⁻³¹.

15
16 The inhibited AMPAR LBD layer is markedly different than the activated state (**Fig. 3a**). While the
17 individual LBDs in each protomer share the same Glu-bound conformation (**Fig. 3b**), the LBD
18 dimers undergo a significant conformational change to accommodate AMPAR inhibition. To
19 assess the changes, we measured the distances between the D1-D1 and D2-D2 in LBD local
20 dimers, which are major indicators of the functional state of the AMPAR²⁹. For example, during
21 activation, the distances between D1's in LBD local dimers are decreased as the D2's separate
22 to pull open the ion channel (**Fig. 1a**). During desensitization, the opposite occurs, where the D1's
23 separate, and the D2 interface is minimized, which decouples Glu binding from the channel, which
24 allows it to close (**Fig. 1a**). The D1 and D2 interfaces in the resting state of the receptor represent
25 an intermediate between the extremes of activation and desensitization.

26
27 In IS-1, we measured the distances between the C α atoms of S741 (D1 separation) and between
28 the C α atoms of S635 (D2 separation) (**Fig. 3c**). The D1 interface is markedly separated (27 Å)
29 compared to the D2 interface (16 Å). To assess how these separations fit with the conformational
30 landscape of existing AMPAR structures in the protein data bank (pdb), we measured D1 and D2
31 separation in AMPAR structures deposited in the pdb (**Fig. 3d**). Generally, structures with a ~26
32 Å or greater distance between S741 in D1 residues represent a desensitized state, while
33 structures with a ~27 Å or greater distance between S635 in D2 represent an active state, with
34 resting state structures representing a medium between the two separations. The activated state
35 of AMPAR is exemplified by pdb 5WEO, resting state pdb 3KG2, and desensitized state pdb
36 5VHZ (all pdb's are mapped in **Extended Data Fig. 7**). The significant rupturing of the D1
37 interfaces in both IS-1 and IS-2 places these LBD dimers squarely into the desensitized
38 classification of LBD dimers. Critically, existing PPLM-bound structures in the pdb represent the
39 resting state of the receptor because they are not Glu-bound (**Fig. 3d**). This is marked by
40 significant differences across the receptors between the PPLM-bound apo states and the inhibited
41 states from this study (**Extended Data Fig. 2b**).

42
43 While the LBDs in local dimers are in a desensitized-like state, the total motion of the LBD layer
44 reveals that inhibition is unique from desensitization. During desensitization, the A/C subunits roll
45 away from their B/D partners to facilitate separation within the local dimers and decouple Glu
46 binding from the ion channel^{18,32} (**Fig. 3e**). In inhibition, we observe the opposite (**Fig. 3e**). During
47 inhibition, the B/D LBDs rotate 21° counterclockwise away from their A/C counterparts, which
48 appear to maintain the position that they assume in the active state (**Fig. 3e**). Therefore, like their
49 role in activation, the B/D subunits drive inhibition. We expect that because the M3 helix kink is
50 prevented by GYKI-52466 in the B/D subunits (**Fig. 3a**), this drives rearrangement in the LBD by
51 the same subunits to accommodate inhibition.

1
2 *Allosteric Competition to Control the AMPAR LBD*

3
4 The positive allosteric modulator CTZ is absent in both our inhibited-state cryo-EM
5 reconstructions despite being included during preparation. This suggests that GYKI-52466, a
6 negative allosteric modulator that binds in the AMPAR TMD, outcompetes CTZ, which binds
7 between AMPAR LBDs, to allosterically control AMPAR function. The absence of CTZ in our cryo-
8 EM reconstructions may be explained by the separation of the D1-D1 interface that we observe
9 in the inhibited state (**Fig. 4a**), which effectively ruptures the CTZ binding pocket (**Fig. 4b**). CTZ
10 binding between AMPAR LBDs at the D1-D1 interface stabilizes D2-D2 separation and prevents
11 desensitization. However, inhibition by GYKI-52466 prevents CTZ from stabilizing the D1-D1
12 interface as the CTZ binding site is completely ruptured in inhibition.

13
14 We therefore postulated that the negative allosteric modulator GYKI-52466 and the positive
15 allosteric modulator CTZ might compete for influence over AMPAR gating, despite binding at
16 disparate sites, with GYKI-52466 exerting greater influence than CTZ when both are at saturating
17 concentration in the preparation. We refer to such a paradigm as allosteric competition.

18
19 To directly test the effects of negative and positive allosteric modulation on the D1-D1 interface,
20 we directly assayed the separation of the D1-D1 interface with smFRET. We achieved this with
21 the mutation L467C at the top of D1 to enable attachment of a dye by maleamide chemistry and
22 establish FRET pairs at the top of the GluA2 LBD³³ (**Fig. 4c**). Labeling GluA2 homotetrameric
23 AMPARs at L467C is ideal for measuring distances within LBD dimers; the FRET efficiency when
24 GluA2 is in the activated state (Glu + CTZ) is expected to be ~92% within an LBD dimer and
25 ~19% across dimer pairs when Alexa-555 and Alexa-647 are used as the donor-acceptor pair³⁴.

26
27 We tested coupling of the D1 interface in our GluA2-TARPy2 construct during positive allosteric
28 modulation in the presence of both 1 mM Glu and 100 μ M CTZ (**Fig. 4d**), where the D1s between
29 LBD dimer pairs are at their closest³⁴⁻³⁶ (**Fig. 4b**). The Glu and CTZ smFRET efficiency histogram
30 shows higher efficiency than receptors in negative allosteric modulation (1 mM Glu and 100 μ M
31 GYKI-52466; **Fig. 4d**). This indicates that the distance across the D1 interface is shorter in the
32 presence of the positive modulator CTZ than in the presence of the negative modulator GYKI-
33 52466. To test that the decrease in smFRET efficiency in inhibitory conditions is AMPAR-
34 dependent and not TARP-dependent, we also tested smFRET efficiency in GluA2 homotetramers
35 in the absence of TARPy2 (**Fig. 4e**). A similar effect is seen between positive allosteric (Glu +
36 CTZ) and negative allosteric (Glu + GYKI-52466) conditions with GluA2 alone, which points to the
37 decrease in smFRET efficiency not being TARP-dependent but GYKI-52466 or CTZ dependent.

38
39 The individual smFRET traces show that the protein occupies 2-3 FRET efficiency states
40 (**Extended Data Fig. 8**) with the most probable state having a FRET efficiency of 0.93 in the
41 presence of cyclothiazide and 0.82 in the presence of GYKI (**Extended Data Fig. 8**). These FRET
42 efficiencies correspond to distances of 33 Å and 39 Å, respectively. The distance change of 6 Å
43 agrees with our IS-1 and IS-2 cryo-EM structures which show a D1-D1 (L467) distance change
44 of 6 Å when compared to the CTZ-bound, activate state AMPAR structure¹⁵. Thus, separation of
45 the D1s in AMPAR LBD dimers appears to be due to negative allosteric modulation by GYKI-
46 52466.

47
48 Collectively, our observations from smFRET and cryo-EM suggest that negative and positive
49 allosteric modulation occupy dramatically different conformational states. The differences
50 between the conformational spaces in each state are a potential mechanism for allosteric
51 competition between the two modulators (**Fig. 4a,b**). Thus, we hypothesized that the negative

1 allosteric effects of GYKI-52466 would outcompete CTZ's positive allosteric modulation on
2 AMPARs. This would be reflected in GYKI-52466 negating CTZ's non-desensitizing effects that
3 CTZ has on AMPAR currents.

4
5 We tested whether GYKI-52466 could overcome the positive allosteric effect CTZ has on
6 AMPARs by patch clamp electrophysiology of HEK293 cells expressing GluA2-TARPy2 (**Fig. 4f**).
7 In the absence of CTZ, the currents rapidly desensitize when treated with 1 mM Glu, and
8 desensitization is completely ablated with 100 μ M CTZ. However, the effect of CTZ on
9 desensitization is negated by 100 μ M GYKI-52466. Thus, the inhibitory effect of GYKI-52466 on
10 AMPARs outcompetes the positive effect that CTZ has on AMPAR currents. We complemented
11 the observation that GYKI-52466 has greater control on AMPAR allostery than CTZ with dose-
12 response curves (**Fig. 4g**). This data shows that GYKI inhibits GluA2-mediated currents even in
13 the presence of excess CTZ; at \sim 3x CTZ concentration, GYKI-52466 inhibits 50% of AMPAR
14 currents (**Fig. 4g**). The IC_{50} of GYKI-52466 in the presence of CTZ was determined to be $39.87 \pm$
15 6.75μ M ($p = .00022$). This is a \sim 10x reduction of the IC_{50} compared to GYKI-52466 alone on
16 AMPAR-TARP complexes³⁷, which aligns well with the observed 10x reduction in GYKI-52466
17 IC_{50} on AMPARs in the presence of CTZ^{26,38,39}.

18
19 While our electrophysiology data agrees with previously reported observations, our data in the
20 context of our observations from cryo-EM and smFRET demonstrates that GYKI-52466 binding
21 in the TMD outcompetes CTZ binding in the LBD for allosteric control of AMPARs.

22 23 *Free Energy Landscape Governing Rupture of the LBD Dimer Interface*

24
25 Comparison of singular inter-residue distances may not account for how inhibition and
26 desensitization occupy similar conformations within LBD dimers but an overall distinct
27 conformation in the overall LBD tetramer^{27,40-43} (**Fig. 3e**). We hypothesized that this may be due
28 to distinct free energy minima accompanying inhibition and desensitization. To test this, we
29 computed a two-dimensional free energy landscape, or potential of mean force (PMF), governing
30 rupture of a Glu-bound GluA2 LBD dimer interface using umbrella sampling free energy molecular
31 dynamics (MD) simulations.

32
33 Our PMF is a function of a two-dimensional order parameter (χ_1 and χ_2) that reports global
34 changes within an LBD dimer. χ_1 and χ_2 describe the distances between the center of mass of
35 helix J in D1 and the center of mass of helix D in D1 on a partner LBD in the dimer (**Fig. 5a**). (χ_1 ,
36 χ_2) differs from the one-dimensional collective variable previously used by to examine LBD dimer
37 stabilities in AMPARs and kainate receptors via steered MD simulations⁴⁴. While the LBDs are
38 generally symmetric, the order parameter is not (**Fig. 5a**); χ_1 describes the helix J and D distance
39 that is exterior facing, while in the context of a tetramer, χ_2 describes the helix pair that faces the
40 interior of the AMPAR. Thus, this enables a two-dimensional approach to characterizing global
41 changes in the LBD dimers.

42
43 Through sampling χ_1 and χ_2 in the context of Glu-bound LBDs, we can understand the energetics
44 associated with rupturing the D1-D1 interface. Conformers for the umbrella sampling windows
45 were generated using targeted MD simulations initiated from the crystal structure of an activated
46 GluA2 LBD and using the crystal structure of a desensitized GluA2 LBD as a guide (**Fig. 5a**; see
47 Methods)^{45,46}. Sampling windows were established in 1 Å increments along χ_1 and χ_2 . The
48 activated state LBD dimer occupies a small free energy basin within the PMF, whereas the fully
49 desensitized LBD occupies a significantly larger basin (**Fig. 5b**). The crystallized desensitized
50 LBD, stabilized by a disulfide bond, lies near the most probable transition pathway between the

1 active and desensitized conformations. This pathway suggests that during rupture of the dimer
2 interface, one J-D helix pair breaks before the other rather than both pairs breaking
3 simultaneously, thereby circumventing a free energy barrier separating the two basins. The
4 broader free energy basin associated with desensitization compared with activation may account
5 for how short-lived the active state is compared to the longer-lived desensitized state.

6
7 A point mutation, L483Y in helix D, had been identified to strongly stabilize the non-desensitized
8 (active) state⁴⁷. To test whether our umbrella sampling strategy could recapitulate the effect of
9 this mutation, we performed an analogous free energy calculation using the GluA2-L483Y LBD
10 dimer. Umbrella sampling window conformers were generated from the crystal structure of the
11 L483Y LBD dimer²². The PMF of this non-desensitizing mutant reveals a substantially reduced
12 free energy basin for the desensitized state, transforming the active state basin into the global
13 free energy minimum (**Extended Data Fig. 9**).

14
15 In inhibition, we observe separation of χ_1 and χ_2 compared to the activated LBD dimer (**Fig. 5a**).
16 Interestingly, this likely occupies a PMF basin that is distinct from the pathway of desensitization
17 (**Fig. 5b**). This supports the observation that inhibition is similar, but distinct, from desensitization.
18 The two-dimensional order parameter that we sample in this experiment accounts for how the
19 LBDs within a dimer pivot away from each other to accommodate D1 separation. We hypothesize
20 that the distinct free energy basins of inhibited and desensitized LBDs account for the differences
21 we observe in the overall motion in the LBD tetramer during inhibition and desensitization (**Fig.**
22 **3e**).

23 **Discussion**

24
25
26 Allosteric modulation of AMPARs is a critical avenue for small molecule therapeutics to regulate
27 AMPAR function. While mechanisms for positive allosteric modulation have been determined prior
28 to this work, the mechanisms of allosteric inhibition by negative allosteric modulators have
29 remained unknown. In addition, we outline how negative and positive modulators can compete in
30 what we term allosteric competition. To our knowledge, this is the first description of allosteric
31 competition in AMPARs, iGluRs, and ligand gated ion channels. We delineate the principles of
32 allosteric competition and negative allosteric modulation with cryo-EM, smFRET,
33 electrophysiology, and molecular dynamics. Elucidation of these details complete our knowledge
34 of the allosteric landscape and provide foundations for structure-based drug design.

35
36 Indeed, despite the central role of AMPARs in neuronal signaling and their role in disease,
37 therapeutic development against AMPARs has remained challenging. This is reflected by only a
38 single AMPAR-targeting drug, perampanel, being approved in the United States and Europe.
39 Over 400,000 people have been prescribed this drug across all indications⁴⁸. Despite this, the
40 perampanel mechanism of action has remained unknown until this study. Perampanel, like GYKI-
41 52466, and other PPLMs, bind to AMPARs in the ion channel collar region and inhibit AMPARs.
42 Our data show that noncompetitive inhibitors do not simply inhibit the activation of AMPARs by
43 keeping the receptor in the resting state^{9,26} but instead inhibit the receptor by decoupling Glu
44 binding from channel opening by pushing the receptor into a desensitized-like state (**Fig. 6a**). The
45 inhibited states (IS-1 and IS-2, this study) show marked differences compared to AMPAR
46 structures bound to PPLMs in the resting state (**Extended Data Fig. 2b**). There are major
47 differences in the separation of the D1-D1 interface (**Fig. 3d**) and overall LBD layer, though the
48 TMD and ATD are similar (**Extended Data Fig. 2b**).

49
50 Supporting our inhibition mechanism are previous studies that suggested a two-step mechanism
51 of inhibition, where an initial binding event by PPLMs is insufficient to produce complete

1 inhibition^{49,50}. These findings support our results, where a two-step mechanism would constitute
2 GYKI-52466 binding followed by Glu binding in the LBDs and rupturing of the D1 interface within
3 LBD dimers. This demonstrates how binding of PPLMs in the ion channel collar allosterically
4 controls the AMPAR ECD (**Fig. 6a**). The evidence for inhibition occupying a similar but distinct
5 mechanism to desensitization also provides new data to conceptualize therapeutically targeting
6 AMPARs. For example, the B/D subunit position domain motion that accompanies inhibition (**Fig.**
7 **3e**) may provide a route for specificity in small molecule targeting considering that these positions
8 are enriched for specific GluA subunits in native AMPARs^{51–53}.

9
10 Our structural data predict that the mechanism of inhibition by PPLMs is independent of auxiliary
11 subunit occupancy of AMPARs. This prediction agrees with our smFRET data showing similar
12 shifts in FRET efficiency in the presence or absence of TARPγ2 in the AMPAR (**Fig. 4b**).
13 However, noncompetitive inhibition of AMPARs may function similarly across different drug types.
14 AMPARs are tightly regulated by TARPs and other auxiliary subunits^{23,24,28,32,54–56} and recently
15 identified compounds demonstrate selectivity for particular AMPAR-TARP complexes^{57–62}.
16 Structural investigations of the binding sites reveal that drug binding of TARP-dependent inhibitors
17 is at a site distinct from that of PPLMs; the site is within the interface between TARPs and AMPAR
18 transmembrane helices. It is possible that these TARP-dependent noncompetitive inhibitors also
19 act as negative allosteric modulators by forcing receptors into a desensitized-like state to achieve
20 inhibition, despite having binding sites distinct from PPLMs. However, resolving this question will
21 require additional studies with AMPARs activated in the presence of the TARP-dependent
22 noncompetitive inhibitors.

23
24 A key observation from our data is the competing mechanisms of positive allosteric modulators
25 (e.g., CTZ) and negative allosteric modulators (e.g., PPLMs). CTZ positively modulates AMPAR
26 function by bringing together the D1-D1 interface in LBD dimers (**Fig. 6a**). Thus, GYKI-52466 and
27 CTZ have been consistently reported to produce opposing effects on channel conductance^{9–11,63}.
28 Early studies postulated that GYKI-52466 and CTZ bind to the same site on AMPARs, owing to
29 their countervailing effects on AMPAR channel conductance^{63,64}. However, subsequent structural
30 and physiological data revealed that CTZ and PPLMs act at distinct sites^{9,26,65}, thereby rendering
31 their mechanistic competition unclear.

32
33 Our data indicate that negative allosteric modulators such as GYKI-52466 can outcompete
34 positive allosteric modulators that bind to a completely distinct site such as CTZ. Indeed, both
35 PPLMs and CTZ can bind to resting state AMPARs^{9,15,23,25,49,66,67}. This allosteric competition (**Fig.**
36 **6b**) to control AMPAR function is a new way to understanding allosteric modulation and allosteric
37 competition in ligand-gated ion channels. This idea was alluded to in early studies on the interplay
38 between GYKI-52466 and CTZ^{26,39}. It was suggested that there is a negative allosteric effect from
39 GYKI-52466 that does not prevent CTZ binding, but instead alters the effect of CTZ on AMPAR
40 desensitization. Our work shows that negative allosteric modulation by GYKI-52466 prevents CTZ
41 from positively modulating AMPARs through rupturing the CTZ binding site. The competing
42 mechanisms of PPLMs such as GYKI-52466 and CTZ may provide a route to fine tune the
43 behavior of AMPARs¹¹.

44
45 Our data reveal that inhibition is a distinct state from the resting state (**Fig. 3e**), but because
46 individual inhibited channels bypass the open state entirely to arrive at the inhibited state, no
47 current is passed and therefore this state is not detectable with electrophysiological analysis other
48 than a reduction in peak current amplitude in whole cell recordings. Thus, our proposed
49 mechanism bridges electrophysiological studies of GYKI-52466 and PPLM competition with CTZ
50 with the structural identification of PPLM binding sites. Furthermore, the revealed details of the
51 GYKI-52466 binding site allow us to disambiguate the arrangement and contribution of sidechains

1 in the PPLM binding pocket that were previously described⁹. Consistent with mutagenesis studies
2 conducted in the PPLM binding pocket⁹, we can confirm the direct interaction of key sidechains
3 that reduced inhibition efficiency following mutation, including S516, P520, S615, F623 and N791
4 as well the likely involvement of N619 in stabilizing GYKI-52466 specifically. Importantly, water
5 molecules may play an important role in the coordination of small molecules in this binding pocket
6 (**Extended Data Fig. 6e**). While the residues that coordinate GYKI-52466 are largely conserved
7 across AMPAR subunits (**Extended Data Fig. 10**), the high-resolution details outlined here, and
8 identification of the negative allosteric modulation mechanism, will improve small molecule design
9 in future studies.

10
11 In sum, we reveal the mechanism of action of how AMPARs are allosterically inhibited and how
12 a new phenomenon of allosteric competition can occur within AMPARs. Our data provide
13 foundations for structure-based drug design against AMPARs as well as a framework to study the
14 mechanism of action of noncompetitive inhibition in other ligand-gated ion channels.

15 16 17 **References**

- 18
19 1. Herculano-Houzel, S. The remarkable, yet not extraordinary, human brain as a scaled-up
20 primate brain and its associated cost. *Proceedings of the National Academy of Sciences* **109**,
21 10661–10668 (2012).
- 22 2. Diering, G. H. & Huganir, R. L. The AMPA Receptor Code of Synaptic Plasticity. *Neuron* **100**,
23 314–329 (2018).
- 24 3. Somogyi, P., Tamás, G., Lujan, R. & Buhl, E. H. Salient features of synaptic organisation in
25 the cerebral cortex1Published on the World Wide Web on 3 March 1998.1. *Brain Research*
26 *Reviews* **26**, 113–135 (1998).
- 27 4. Hansen, K. B. *et al.* Structure, Function, and Pharmacology of Glutamate Receptor Ion
28 Channels. *Pharmacol Rev* **73**, 298–487 (2021).
- 29 5. Hanada, T. *et al.* Perampanel: A novel, orally active, noncompetitive AMPA-receptor
30 antagonist that reduces seizure activity in rodent models of epilepsy. *Epilepsia* **52**, 1331–
31 1340 (2011).
- 32 6. Greenwood, J. & Valdes, J. Perampanel (Fycompa). *P T* **41**, 683–698 (2016).
- 33 7. Tarnawa, I., Farkas, S., Berzsenyi, P., Pataki, Á. & András, F. Electrophysiological studies
34 with a 2,3-benzodiazepine muscle relaxant: GYKI 52466. *European Journal of Pharmacology*
35 **167**, 193–199 (1989).
- 36 8. Donevan, S. D. & Rogawski, M. A. GYKI 52466, a 2,3-benzodiazepine, is a highly selective,
37 noncompetitive antagonist of AMPA/kainate receptor responses. *Neuron* **10**, 51–59 (1993).
- 38 9. Yelshanskaya, M. V. *et al.* Structural Bases of Noncompetitive Inhibition of AMPA-Subtype
39 Ionotropic Glutamate Receptors by Antiepileptic Drugs. *Neuron* **91**, 1305–1315 (2016).
- 40 10. Rammes, G., Swandulla, D., Spielmanns, P. & Parsons, C. G. Interactions of GYKI 52466
41 and NBQX with cyclothiazide at AMPA receptors: experiments with outside-out patches and
42 EPSCs in hippocampal neurones. *Neuropharmacology* **37**, 1299–1320 (1998).
- 43 11. Shi, E. Y. *et al.* Noncompetitive antagonists induce cooperative AMPA receptor channel
44 gating. *J Gen Physiol* **151**, 156–173 (2019).
- 45 12. Sullivan, B. J. *et al.* Low-Dose Perampanel Rescues Cortical Gamma Dysregulation
46 Associated With Parvalbumin Interneuron GluA2 Upregulation in Epileptic Syngap1+/- Mice.
47 *Biological Psychiatry* **87**, 829–842 (2020).
- 48 13. Yang, Y.-C., Wang, G.-H., Chuang, A.-Y. & Hsueh, S.-W. Perampanel reduces paroxysmal
49 depolarizing shift and inhibitory synaptic input in excitatory neurons to inhibit epileptic
50 network oscillations. *British Journal of Pharmacology* **177**, 5177–5194 (2020).

- 1 14. Rugg-Gunn, F. Adverse effects and safety profile of perampanel: A review of pooled data.
2 *Epilepsia* **55**, 13–15 (2014).
- 3 15. Twomey, E. C., Yelshanskaya, M. V., Grassucci, R. A., Frank, J. & Sobolevsky, A. I. Channel
4 opening and gating mechanism in AMPA-subtype glutamate receptors. *Nature* **549**, 60–65
5 (2017).
- 6 16. Chen, S. *et al.* Activation and Desensitization Mechanism of AMPA Receptor-TARP Complex
7 by Cryo-EM. *Cell* **170**, 1234–1246.e14 (2017).
- 8 17. Dürr, K. L. *et al.* Structure and Dynamics of AMPA Receptor GluA2 in Resting, Pre-Open,
9 and Desensitized States. *Cell* **158**, 778–792 (2014).
- 10 18. Twomey, E. C., Yelshanskaya, M. V., Grassucci, R. A., Frank, J. & Sobolevsky, A. I.
11 Structural Bases of Desensitization in AMPA Receptor-Auxiliary Subunit Complexes. *Neuron*
12 **94**, 569–580.e5 (2017).
- 13 19. Hoyt, K. R., Rajdev, S., Fattman, C. L. & Reynolds, I. J. Cyclothiazide modulates AMPA
14 receptor-mediated increases in intracellular free Ca²⁺ and Mg²⁺ in cultured neurons from rat
15 brain. *J Neurochem* **64**, 2049–2056 (1995).
- 16 20. Patneau, D., Vyklicky, L. & Mayer, M. Hippocampal neurons exhibit cyclothiazide-sensitive
17 rapidly desensitizing responses to kainate. *J Neurosci* **13**, 3496–3509 (1993).
- 18 21. Yamada, K. A. & Tang, C. M. Benzothiadiazides inhibit rapid glutamate receptor
19 desensitization and enhance glutamatergic synaptic currents. *J Neurosci* **13**, 3904–3915
20 (1993).
- 21 22. Sun, Y. *et al.* Mechanism of glutamate receptor desensitization. *Nature* **417**, 245–253 (2002).
- 22 23. Gangwar, S. P. *et al.* Modulation of GluA2–γ5 synaptic complex desensitization, polyamine
23 block and antiepileptic perampanel inhibition by auxiliary subunit cornichon-2. *Nat Struct Mol*
24 *Biol* **30**, 1481–1494 (2023).
- 25 24. Twomey, E. C., Yelshanskaya, M. V., Grassucci, R. A., Frank, J. & Sobolevsky, A. I.
26 Elucidation of AMPA receptor-stargazin complexes by cryo-electron microscopy. *Science*
27 **353**, 83–86 (2016).
- 28 25. Yelshanskaya, M. V., Patel, D. S., Kottke, C. M., Kurnikova, M. G. & Sobolevsky, A. I.
29 Opening of glutamate receptor channel to subconductance levels. *Nature* **605**, 172–178
30 (2022).
- 31 26. Balannik, V., Menniti, F. S., Paternain, A. V., Lerma, J. & Stern-Bach, Y. Molecular
32 Mechanism of AMPA Receptor Noncompetitive Antagonism. *Neuron* **48**, 279–288 (2005).
- 33 27. Salazar, H., Mischke, S. & Plested, A. J. R. Measurements of the Timescale and
34 Conformational Space of AMPA Receptor Desensitization. *Biophysical Journal* **119**, 206–218
35 (2020).
- 36 28. Zhang, D., Watson, J. F., Matthews, P. M., Cais, O. & Greger, I. H. Gating and modulation of
37 a hetero-octameric AMPA glutamate receptor. *Nature* **594**, 454–458 (2021).
- 38 29. Twomey, E. C. & Sobolevsky, A. I. Structural Mechanisms of Gating in Ionotropic Glutamate
39 Receptors. *Biochemistry* **57**, 267–276 (2018).
- 40 30. Tomita, S., Shenoy, A., Fukata, Y., Nicoll, R. A. & Brecht, D. S. Stargazin interacts functionally
41 with the AMPA receptor glutamate-binding module. *Neuropharmacology* **52**, 87–91 (2007).
- 42 31. Díaz-Alonso, J. *et al.* Subunit-specific role for the amino-terminal domain of AMPA receptors
43 in synaptic targeting. *Proceedings of the National Academy of Sciences* **114**, 7136–7141
44 (2017).
- 45 32. Klykov, O., Gangwar, S. P., Yelshanskaya, M. V., Yen, L. & Sobolevsky, A. I. Structure and
46 desensitization of AMPA receptor complexes with type II TARP γ5 and GSG1L. *Molecular*
47 *Cell* **81**, 4771–4783.e7 (2021).
- 48 33. Carrillo, E. *et al.* Mechanism of modulation of AMPA receptors by TARP-γ8. *J Gen Physiol*
49 **152**, e201912451 (2019).
- 50 34. Carrillo, E. *et al.* Mechanism of modulation of AMPA receptors by TARP-γ8. *Journal of*
51 *General Physiology* **152**, jgp.201912451 (2019).

- 1 35. Landes, C. F., Rambhadran, A., Taylor, J. N., Salatan, F. & Jayaraman, V. Structural
2 landscape of isolated agonist-binding domains from single AMPA receptors. *Nat Chem Biol*
3 **7**, 168–173 (2011).
- 4 36. Shaikh, S. A. *et al.* Stargazin Modulation of AMPA Receptors. *Cell Reports* **17**, 328–335
5 (2016).
- 6 37. Knopp, K. L. *et al.* Modulation of TARP γ 8-Containing AMPA Receptors as a Novel
7 Therapeutic Approach for Chronic Pain. *J Pharmacol Exp Ther* **369**, 345–363 (2019).
- 8 38. Donevan, S. D. & Rogawski, M. A. Allosteric regulation of alpha-amino-3-hydroxy-5-methyl-4-
9 isoxazole-propionate receptors by thiocyanate and cyclothiazide at a common modulatory
10 site distinct from that of 2,3-benzodiazepines. *Neuroscience* **87**, 615–629 (1998).
- 11 39. Palmer, A. J. & Lodge, D. Cyclothiazide reverses AMPA receptor antagonism of the 2,3-
12 benzodiazepine, GYKI 53655. *Eur J Pharmacol* **244**, 193–194 (1993).
- 13 40. Lau, A. Y. Enhanced sampling of glutamate receptor ligand-binding domains. *Neurosci Lett*
14 **700**, 17–21 (2019).
- 15 41. Lau, A. Y. & Roux, B. The Hidden Energetics of Ligand-Binding and Activation in a Glutamate
16 Receptor. *Nat Struct Mol Biol* **18**, 283–287 (2011).
- 17 42. Yu, A., Wied, T., Belcher, J. & Lau, A. Y. Computing Conformational Free Energies of iGluR
18 Ligand-Binding Domains. in *Ionotropic Glutamate Receptor Technologies* (ed. Popescu, G.
19 K.) 119–132 (Springer, 2016). doi:10.1007/978-1-4939-2812-5_9.
- 20 43. Baranovic, J. *et al.* Dynamics of the Ligand Binding Domain Layer during AMPA Receptor
21 Activation. *Biophys J* **110**, 896–911 (2016).
- 22 44. Musgaard, M. & Biggin, P. C. Steered Molecular Dynamics Simulations Predict
23 Conformational Stability of Glutamate Receptors. *J Chem Inf Model* **56**, 1787–1797 (2016).
- 24 45. Armstrong, N. & Gouaux, E. Mechanisms for Activation and Antagonism of an AMPA-
25 Sensitive Glutamate Receptor: Crystal Structures of the GluR2 Ligand Binding Core. *Neuron*
26 **28**, 165–181 (2000).
- 27 46. Armstrong, N., Jasti, J., Beich-Frandsen, M. & Gouaux, E. Measurement of Conformational
28 Changes accompanying Desensitization in an Ionotropic Glutamate Receptor. *Cell* **127**, 85–
29 97 (2006).
- 30 47. Stern-Bach, Y., Russo, S., Neuman, M. & Rosenmund, C. A point mutation in the glutamate
31 binding site blocks desensitization of AMPA receptors. *Neuron* **21**, 907–918 (1998).
- 32 48. FYCOMPA® (perampanel) CIII: Treatment for Partial-Onset (4 yrs+) & PGTC (12 yrs+)
33 Seizures. <https://www.fycompa.com/>.
- 34 49. Ritz, M., Wang, C., Micale, N., Ettari, R. & Niu, L. Mechanism of Inhibition of the GluA2
35 AMPA Receptor Channel Opening: the Role of 4-Methyl versus 4-Carbonyl Group on the
36 Diazepine Ring of 2,3-Benzodiazepine Derivatives. *ACS Chem Neurosci* **2**, 506–513 (2011).
- 37 50. Ritz, M., Micale, N., Grasso, S. & Niu, L. Mechanism of Inhibition of the GluR2 AMPA
38 Receptor Channel Opening by 2,3-Benzodiazepine Derivatives. *Biochemistry* **47**, 1061–1069
39 (2008).
- 40 51. Zhao, Y., Chen, S., Swensen, A. C., Qian, W.-J. & Gouaux, E. Architecture and subunit
41 arrangement of native AMPA receptors elucidated by cryo-EM. *Science* **364**, 355–362
42 (2019).
- 43 52. Yu, J. *et al.* Hippocampal AMPA receptor assemblies and mechanism of allosteric inhibition.
44 *Nature* **594**, 448–453 (2021).
- 45 53. Rao, P. & Gouaux, E. Purification and biochemical analysis of native AMPA receptors from
46 three different mammalian species. *PLOS ONE* **18**, e0275351 (2023).
- 47 54. Zhang, D. *et al.* Structural mobility tunes signalling of the GluA1 AMPA glutamate receptor.
48 *Nature* **621**, 877–882 (2023).
- 49 55. Nakagawa, T. Structures of the AMPA receptor in complex with its auxiliary subunit
50 cornichon. *Science* **366**, 1259–1263 (2019).

- 1 56. Zhang, D. *et al.* Structural mobility tunes signalling of the GluA1 AMPA glutamate receptor.
2 *Nature* **621**, 877–882 (2023).
- 3 57. Gardinier, K. M. *et al.* Discovery of the First α -Amino-3-hydroxy-5-methyl-4-
4 isoxazolepropionic Acid (AMPA) Receptor Antagonist Dependent upon Transmembrane
5 AMPA Receptor Regulatory Protein (TARP) γ -8. *J Med Chem* **59**, 4753–4768 (2016).
- 6 58. Kato, A. S. *et al.* Forebrain-selective AMPA-receptor antagonism guided by TARP γ -8 as an
7 antiepileptic mechanism. *Nat Med* **22**, 1496–1501 (2016).
- 8 59. Maher, M. P. *et al.* Discovery and Characterization of AMPA Receptor Modulators Selective
9 for TARP- γ 8. *J Pharmacol Exp Ther* **357**, 394–414 (2016).
- 10 60. Savall, B. M. *et al.* Discovery of Imidazo[1,2-a]pyrazines and Pyrazolo[1,5-c]pyrimidines as
11 TARP γ -8 Selective AMPAR Negative Modulators. *ACS Med Chem Lett* **10**, 267–272 (2019).
- 12 61. Ravula, S. *et al.* Lead Optimization of 5-Aryl Benzimidazolone- and Oxindole-Based AMPA
13 Receptor Modulators Selective for TARP γ -8. *ACS Med Chem Lett* **9**, 821–826 (2018).
- 14 62. Zhang, D. *et al.* Modulatory mechanisms of TARP γ 8-selective AMPA receptor therapeutics.
15 *Nat Commun* **14**, 1659 (2023).
- 16 63. Zorumski, C. F., Yamada, K. A., Price, M. T. & Olney, J. W. A benzodiazepine recognition
17 site associated with the non-NMDA glutamate receptor. *Neuron* **10**, 61–67 (1993).
- 18 64. Barnes, J. M., Dev, K. K. & Henley, J. M. Cyclothiazide unmasks AMPA-evoked stimulation of
19 [3H]-L-glutamate release from rat hippocampal synaptosomes. *Br J Pharmacol* **113**, 339–341
20 (1994).
- 21 65. Sun, Y. *et al.* Mechanism of glutamate receptor desensitization. *Nature* **417**, 245–253 (2002).
- 22 66. Wang, C., Han, Y., Wu, A., Solyom, S. & Niu, L. Mechanism and Site of Inhibition of AMPA
23 Receptors: Pairing a Thiadiazole with a 2,3-Benzodiazepine Scaffold. *ACS Chem. Neurosci.*
24 **5**, 138–147 (2014).
- 25 67. Wu, A., Wang, C. & Niu, L. Mechanism of inhibition of the GluA1 AMPA receptor channel
26 opening by the 2,3-benzodiazepine compound GYKI 52466 and a N-methyl-carbamoyl
27 derivative. *Biochemistry* **53**, 3033–3041 (2014).
- 28 68. Twomey, E. C., Yelshanskaya, M. V., Vassilevski, A. A. & Sobolevsky, A. I. Mechanisms of
29 Channel Block in Calcium-Permeable AMPA Receptors. *Neuron* **99**, 956-968.e4 (2018).
- 30 69. Goehring, A. *et al.* Screening and large-scale expression of membrane proteins in
31 mammalian cells for structural studies. *Nat Protoc* **9**, 2574–2585 (2014).
- 32 70. Punjani, A., Rubinstein, J. L., Fleet, D. J. & Brubaker, M. A. cryoSPARC: algorithms for rapid
33 unsupervised cryo-EM structure determination. *Nat Methods* **14**, 290–296 (2017).
- 34 71. Tan, Y. Z. *et al.* Addressing preferred specimen orientation in single-particle cryo-EM through
35 tilting. *Nat Methods* **14**, 793–796 (2017).
- 36 72. Pettersen, E. F. *et al.* UCSF ChimeraX: Structure visualization for researchers, educators,
37 and developers. *Protein Science* **30**, 70–82 (2021).
- 38 73. Croll, T. I. ISOLDE: a physically realistic environment for model building into low-resolution
39 electron-density maps. *Acta Crystallogr D Struct Biol* **74**, 519–530 (2018).
- 40 74. Emsley, P. & Cowtan, K. Coot: model-building tools for molecular graphics. *Acta Cryst D* **60**,
41 2126–2132 (2004).
- 42 75. Liebschner, D. *et al.* Macromolecular structure determination using X-rays, neutrons and
43 electrons: recent developments in Phenix. *Acta Cryst D* **75**, 861–877 (2019).
- 44 76. Afonine, P. V. *et al.* Real-space refinement in PHENIX for cryo-EM and crystallography. *Acta*
45 *Crystallogr D Struct Biol* **74**, 531–544 (2018).
- 46 77. Morin, A. *et al.* Collaboration gets the most out of software. *eLife* **2**, e01456 (2013).
- 47 78. Williams, C. J. *et al.* MolProbity: More and better reference data for improved all-atom
48 structure validation. *Protein Science* **27**, 293–315 (2018).
- 49 79. Sehnal, D. *et al.* MOLE 2.0: advanced approach for analysis of biomacromolecular channels.
50 *Journal of Cheminformatics* **5**, 39 (2013).

- 1 80. Durham, R. J. *et al.* Conformational spread and dynamics in allostery of NMDA receptors.
2 *Proceedings of the National Academy of Sciences* **117**, 3839–3847 (2020).
- 3 81. Durham, R. J., Latham, D. R., Sanabria, H. & Jayaraman, V. Structural Dynamics of
4 Glutamate Signaling Systems by smFRET. *Biophys J* **119**, 1929–1936 (2020).
- 5 82. Litwin, D., Durham, R. & Jayaraman, V. Single molecule FRET methods to study Glutamate
6 receptors. *Methods Mol Biol* **1941**, 3–16 (2019).
- 7 83. MacLean, D. M., Durham, R. J. & Jayaraman, V. Mapping the Conformational Landscape of
8 Glutamate Receptors Using Single Molecule FRET. *Trends Neurosci* **42**, 128–139 (2019).
- 9 84. Paudyal, N., Bhatia, N. K. & Jayaraman, V. Single molecule FRET methodology for
10 investigating glutamate receptors. *Methods Enzymol* **652**, 193–212 (2021).
- 11 85. Shuang, B. *et al.* Fast Step Transition and State Identification (STaSI) for Discrete Single-
12 Molecule Data Analysis. *J. Phys. Chem. Lett.* **5**, 3157–3161 (2014).
- 13 86. Brooks, B. R. *et al.* CHARMM: the biomolecular simulation program. *J Comput Chem* **30**,
14 1545–1614 (2009).
- 15 87. Fiser, A. & Sali, A. ModLoop: automated modeling of loops in protein structures.
16 *Bioinformatics* **19**, 2500–2501 (2003).
- 17 88. Krivov, G. G., Shapovalov, M. V. & Dunbrack, R. L. Improved prediction of protein side-chain
18 conformations with SCWRL4. *Proteins* **77**, 778–795 (2009).
- 19 89. MacKerell, A. D. *et al.* All-atom empirical potential for molecular modeling and dynamics
20 studies of proteins. *J Phys Chem B* **102**, 3586–3616 (1998).
- 21 90. Mackerell, A. D., Feig, M. & Brooks, C. L. Extending the treatment of backbone energetics in
22 protein force fields: limitations of gas-phase quantum mechanics in reproducing protein
23 conformational distributions in molecular dynamics simulations. *J Comput Chem* **25**, 1400–
24 1415 (2004).
- 25 91. Jorgensen, W. L., Chandrasekhar, J., Madura, J. D., Impey, R. W. & Klein, M. L. Comparison
26 of simple potential functions for simulating liquid water. *The Journal of Chemical Physics* **79**,
27 926–935 (1983).
- 28 92. Feller, S. E., Zhang, Y., Pastor, R. W. & Brooks, B. R. Constant pressure molecular dynamics
29 simulation: The Langevin piston method. *The Journal of Chemical Physics* **103**, 4613–4621
30 (1995).
- 31 93. Essmann, U. *et al.* A smooth particle mesh Ewald method. *The Journal of Chemical Physics*
32 **103**, 8577–8593 (1995).
- 33 94. Kumar, S., Rosenberg, J. M., Bouzida, D., Swendsen, R. H. & Kollman, P. A. THE weighted
34 histogram analysis method for free-energy calculations on biomolecules. I. The method.
35 *Journal of Computational Chemistry* **13**, 1011–1021 (1992).
- 36 95. Souaille, M. & Roux, B. Extension to the weighted histogram analysis method: combining
37 umbrella sampling with free energy calculations. *Computer Physics Communications* **135**,
38 40–57 (2001).
- 39

1 Figure Legends

2

3 **Figure 1. Structure of the AMPAR inhibited state.** a) Schematic representation of the
4 AMPAR gating cycle. b) Ribbon illustration detailing the structure of the AMPAR inhibited state,
5 IS-1. GluA2 subunits are purple (A/C) or orange (B/D) depending on their positions. GYKI-
6 52466 (pink) is bound at all four TMD collar regions and each LBD clamshell is closed around
7 glutamate (green). TARPγ2 subunits (light blue) occupy all four auxiliary sites around the
8 receptor. c) High resolution details of the focused GluA2 TMD from cryo-EM reconstruction.
9 Side view (top) of the GluA2 TMD from showing the M3 bundle crossing in a closed
10 conformation and top view (bottom) showing the bundle crossing constricting access to the ion
11 channel (green, dashed) and the relative location of the channel collar (yellow, dashed) with
12 GYKI-52466 bound to all four GluA2 subunits. Lipids (blue) adorn the AMPAR TMD. d) Plot of
13 the ion channel radius along the pore axis showing a constriction at the M3 bundle crossing
14 gate. Dashed line represents the radius of a water molecule.

15

16 **Figure 2. High-resolution details of GYKI-52466 binding.** a) GYKI-52466 (gray with pink
17 spheres) makes extensive contact with residues within the TMD collar region (orange ribbons),
18 including interacting with S615 on the neighboring M4 helix counterclockwise from the 'bound'
19 subunit (purple). b) Schematic representation of GYKI-52466 interactions with TMD collar
20 residues. Pi bonds represented by curved lines; Van der Waals interactions represented by
21 dashes. c) Top-down view of the inhibited TMD, showing landmark residues around the GYKI-
22 52466 binding pocket. d) Plot detailing the inter-residue distances between landmark GYKI-
23 52466 binding pocket residues and solvent accessible surface surrounding GYKI-52466.

24

25 **Figure 3. Mechanism of negative allosteric modulation.** a) Overlay of the inhibited state
26 (orange) and the activated state (pdb 5WEO, white). *Inset:* Close-up view of the GYKI-52466
27 binding site revealing a steric clash with the kinked M3 helix found in the open state. b) Overlay
28 of isolated LBD clamshells from the inhibited state (pink) and the open state (white). c) Local
29 clamshell dimers within the LBD layer viewed from behind, showing the relative distances of the
30 D1 and D2 lobes of the LBD dimer as illustrated by the landmark residues S741 (D1) and S635
31 (D2). d) Plot of the D1 distance ($C\alpha$ of S741) versus D2 distance ($C\alpha$ of S635) measured for
32 representative AMPAR structures captured in either the resting, activated, or desensitized state.
33 Based on these measurements, the inhibited states (pink) cluster most closely with the
34 desensitized state structures. e) Overlay of the overall LBD layer of the inhibited state (orange
35 and purple), activated state (white) and desensitized state (blue) viewed from the top or
36 extracellular side. Desensitization causes a 14° clockwise rotation of the A/C subunits within the
37 LBD layer relative to the activated state. In contrast, inhibition drives a counterclockwise rotation
38 of the B/D subunits within the LBD layer relative to the active state.

39

40 **Figure 4. Allosteric Competition in AMPARs.** a) Local LBD clamshell from the inhibited state
41 (IS-1) with landmark residues to show D1 and D2 separation within the dimer. This represents
42 the dimer during negative allosteric modulation. b) Local LBD clamshell dimer activated in the
43 presence of CTZ, showing decreased D1 separation and increased D2 separation. This is
44 indicative of positive allosteric modulation. CTZ shown in blue. Distances measured as in Figure
45 3. c) Top-down view of the LBD layer with L467, where the L467C mutation is used for maleimide
46 dye labeling, marked with a blue sphere and inter-subunit L467-L467 $C\alpha$ distances labeled. d)
47 Plot of FRET efficiency between LBD clamshells within a local dimer when GluA2-TARPγ2 protein
48 was treated with Glu + CTZ alone vs Glu + CTZ + GYKI-52466. e) Same as in d, but with GluA2
49 protein in the absence of TARPγ2. f) Whole-cell patch clamp recordings from HEK293 cells
50 expressing GluA2-TARPγ2 protein in the presence of either Glu, Glu + CTZ, or Glu + CTZ + G

1 YKI-52466. g) Whole-cell patch clamp traces of HEK293 cells expressing GluA2-TARPy2 treated
2 with 1mM Glu + 100 μ M CTZ either alone or with increasing concentrations of GYKI-52466.

3
4 **Figure 5. Free energy landscapes governing desensitization and inhibition.** a) (top) Rear
5 views of local LBD clamshell dimers from the inhibited state, activated state, desensitized state,
6 or a projected maximally desensitized state. (bottom) Top-down views of the inhibited, activated,
7 desensitized, or maximally desensitized states with Helices D and J, colored green, labeled in
8 accordance with their contribution to the 2D order parameter. b) Free energy landscape governing
9 LBD dimer conformations, i.e., the separation of helices D and J at the dimer interface, with the
10 measured distances of the activated (green), desensitized (orange), and maximally desensitized
11 distances (blue) plotted on the diagram. Corresponding measurements from the inhibited state
12 are shown in pink, which corresponds to where we would expect the inhibited state to sit within
13 the free energy landscape. The dashed line suggests the most probable transition pathway
14 between the active and desensitized conformations. The free energy landscape is contoured in 1
15 kcal/mol increments.

16
17 **Figure 6. Allosteric landscape of AMPARs.** a) Activation of AMPARs in the presence of the
18 negative allosteric modulator GYKI-52466 produces the inhibited state, which we show in this
19 study. In contrast, activation of AMPARs in the presence of the positive allosteric modulator CTZ
20 produces the activated state. b) When both CTZ and GYKI-52466 are present, both can bind to
21 the resting state of the receptor, but after Glu binding, GYKI-52466 outcompetes CTZ to control
22 the AMPAR LBD, resulting in CTZ being displaced, and inhibition of the receptor.

23
24 **Extended Data 1. Preparation of GluA2-TARPy2.** a) Coomassie-stained SDS PAGE gel of
25 purified GluA2-TARPy2 sample showing a single band at the predicted molecular weight
26 (arrow). b) Size exclusion chromatogram of purified GluA2-TARPy2 sample showing a single
27 monodispersed peak at the predicted retention time for a GluA2-TARPy2. c) (i) Treatment
28 regimens for producing the different inhibited states IS-1 and IS-2, (ii) cartoon demonstrating the
29 targeted outcome of activating the GluA2-TARPy2 assembly in the presence of the inhibitor
30 GYKI-52466.

31
32 **Extended Data 2. Comparison between inhibited states and AMPAR structures in resting
33 state bound to PPLMs.** a) overlay of IS-1 and IS-2 from this study demonstrating very minor
34 deviation in the two states from each other. b) overlay of IS-1 and IS-2 against crystal structures
35 of GluA2 in complex with PPLMs: CP465022 (PDB: 5L1E), Perampanel (PDB: 5L1F), GYKI-Br
36 (PDB: 5L1G), and GYKI-53655 (PDB: 5L1H). RMSD is greatest within the LBD layer, in
37 agreement with the conformational shifts observed following GluA2-TARPy2 activation in the
38 presence of GYKI-52466.

39
40 **Extended Data 3. Cryo-EM processing workflow for IS-1.**

41
42 **Extended Data 4. Cryo-EM processing workflow for IS-2.**

43
44 **Extended Data 5. Structured lipids stabilize the AMPAR TMD.** Coulomb potential maps of
45 the AMPAR TMD from signal subtraction and focused refinement highlighting the presence of
46 lipids (blue) bound to the TMD. (i) close-up of lipids bound to the B/D TMD subunits of the
47 receptor showing at least seven distinct densities. (ii) close-up of the A/C subunits of the
48 receptor demonstrating similar, but distinct lipid arrangements around the TMD.

49
50 **Extended Data 6. IS-1 Cryo-EM and workflow for elucidating GYKI-52466 binding pocket.**
51 a) Examples of Cryo-EM map for the AMPAR TMD and LBD. b) Symmetry expansion was

1 applied through to the isolated IS-1 TMD to increase the effective particle count of the GYKI-
2 52466 binding pocket. b) Following expansion one of the four GYKI-52466 binding pockets was
3 masked and then the mask inverted to subtract away the remaining TMD structure. c) Local
4 refinement of the isolated GYKI-52466 binding pocket resolved the pocket to 2.21 Å resolution.
5 d) Cryo-EM map of the GYKI-52466 shown from left to right at thresholds of 0.8, 0.6, and
6 0.4. Arrows point to potential water molecules within the binding pocket.

7
8 **Extended Data 7. Clustering of AMPAR structures based on D1 and D2 distances.** A
9 detailed look of how published AMPAR structures cluster based on the measurements between
10 the D1 and D2 lobes of LBD clamshells within local dimers. PDB reference numbers are given
11 for each structure measured.

12
13 **Extended Data 8. smFRET characterization of GYKI-52466 and CTZ allosteric modulation**
14 **of AMPARs.** a) (Top) Representative FRET efficiency traces for sampled four molecules in
15 each condition (1 mM Glu + 100 μM CTZ or GYKI-52466) in GluA2-TARPy2. (Bottom) FRET
16 efficiency histogram generated from the compilation of all analyzed single-molecule traces. b)
17 Same as panel a, but GluA2 without TARPy2. c) Statistical analysis of the smFRET data. Mean
18 of the mode for each day with standard error demonstrates a significant decrease in FRET
19 efficiency from CTZ condition to GYKI-52466 condition using two-sample t-test assuming a one-
20 tail distribution with known variances. *1 day of 30 molecules with 1mM of Glutamate and 100
21 μM CTZ were obtained from Carrillo and Shaikh et al. (2020). d) Concentration dependent
22 inhibition by GYKI of GluA2-TARPy2 residual currents in the presence of 1 mM of Glutamate
23 and 100 μM of CTZ (IC50 = 39.87 ± 6.76 μM).

24
25 **Extended Data 9. Free energy landscape governing desensitization in the GluA2-L483Y**
26 **LBD dimer.** The PMF is computed as a function of (χ_1, χ_2), the two distances between helices D
27 and J at the dimer interface. The PMF is contoured in 1 kcal/mol increments.

28
29 **Extended Data 10. Alignment of GluA subunits.** Multiple sequence alignment of Rat GluA1-4
30 protein sequences. Conservation is indicated by the intensity of purple coloring. Secondary
31 structure is displayed above the alignment. GYKI-52466 interacting residues are highlighted in
32 pink.

1 **Methods**

2

3 *Construct design*

4

5 The fusion construct GluA2-TARPy2 was published previously^{15,18,24,68} and was
6 constructed by fusing the GluA2 cDNA from rat to a GT linker, followed immediately by
7 the N-terminus of mouse TARPy2. The c-terminus of TARPy2 is truncated following M4
8 followed by a Thrombin cleavage site, enhanced GFP (eGFP), and Strep Tag II
9 immediately followed by a stop codon. This construct utilizes the pEG BacMam vector
10 for baculovirus-driven protein expression in mammalian cells⁶⁹.

11

12 For smFRET, the GluA2 construct was designed as previously described³³. Briefly, cysteine
13 residues 89, 196, and 436 were mutated to serines in the GluA2-flip (unedited Q isoform)
14 construct to obtain the cysteine-light GluA2 construct, and a cysteine was introduced at position
15 467 for maleamide dye attachment to measure the intradimer interface of the LBD. To generate
16 the GluA2-TARPy2 construct for smFRET, the TARPy8 from GluA2-TARPy8 construct containing
17 site L467C³³ was replaced with TARPy2 from the GluA2-TARPy2 construct³⁶ using restriction
18 enzyme cloning with restriction enzymes BamHI and EcoRV to generate GluA2-TARPy2 with
19 cysteine site at 467.

20

21 *Protein expression and purification*

22

23 GluA2-TARPy2 bacmid was prepared as previously described^{15,18,24}. P1 baculovirus was
24 generated by transfecting ExpiSf9 cells (Gibco, A35243) cultured at 27 °C with polyethylenimine
25 MW 40,000 (PolyScience, 24765). After 5 days, P1 virus was harvested, and expression in
26 mammalian cells was induced by the addition of P1 baculovirus to Expi293F GnTI- cells (Gibco,
27 A39240) grown in Expi293 media (Gibco, A14135101) in a 1:10 ratio of P1 virus to culture volume.
28 Cells were grown in 37 °C, 5% CO₂. 12-24 hours post-induction, the cell culture media was
29 brought up to 10 mM Sodium Butyrate (Sigma, 303410) and 2 μM ZK 20075 (Tocris, 2345) and
30 moved into a 30 °C, 5% CO₂ incubator. The cells were harvested 72 h after transduction by
31 centrifugation (5,000 g, 20 min at 4 °C) washed with PBS (pH 7.4) with protease inhibitors added
32 (0.8 μM aprotinin, 2 μg ml⁻¹ leupeptin, 2 μM pepstatin A, and 1 mM phenyl-methylsulfonyl fluoride)
33 and then pelleted again (4800 g, 10 min at 4 °C). Supernatant was discarded and pellets were
34 stored at -80 °C until purification. Pellets were thawed rotating in Lysis Buffer (150 mM NaCl, 20
35 mM Tris pH 8.0) with protease inhibitors added. Cells were lysed in an ice bath with a blunt probe
36 sonicator (3 cycles, 1s on, 1s for 1 min, 20 W power). Lysed cells were centrifuged to pellet large
37 cellular debris (4,800 g, 20 min at 4 °C). Supernatant was ultracentrifuged to pellet membranes
38 (125,000 g, 45min), which were solubilized in solubilization buffer (150 mM NaCl, 20 mM Tris pH
39 8.0, 1% n-Dodecyl-β-D-Maltopyranoside (Anatrace, D310) and 0.2% Cholesteryl Hemisuccinate
40 Tris salt (Anatrace, CH210) for 2 hours at 4°C under constant stirring. Insoluble material was
41 pelleted in an ultracentrifuge (125,000 g, 45min at 4 °C) and solubilized protein was incubated
42 with 0.75 mL Streptactin XT 4Flow resin (iba, 2-5010) per 1 L of cells overnight, rotating at 4°C.
43 The following day, the resin was collected via gravity flow, and the resin was washed with 20
44 column volumes of GDN buffer (150 mM NaCl, 20 mM Tris pH 8.0, 0.01% GDN (glycol-diosgenin,
45 Anatrace, GDN101)), before elution in GDN buffer made up to 50 mM D-biotin. Eluate was
46 collected in a centrifugal concentrator and concentrated into a 500 μL volume at 4 °C. To remove
47 eGFP and Strep Tag II, the concentrated protein was incubated with thrombin (1:200 w/w) for 1
48 h at 22 °C. The cleavage reaction was separated over a Superose 6 increase 10/300 column
49 (Cytiva, 29091596) using an AKTA FPLC in GDN buffer. Peak fractions were collected and
50 concentrated to 4.5 mg/ml.

1
2
3
4
5
6
7
8
9
10
11
12
13
14
15
16
17
18
19
20
21
22
23
24
25
26
27
28
29
30
31
32
33
34
35
36
37
38
39
40
41
42
43
44
45
46
47
48
49
50
51

Sample preparation and data collection

UltraAuFoil 300 mesh R 1.2/1.3 grids (Electron Microscopy Services, Q350AR13A) were plasma treated in a Pelco Easiglow (25 mA, 120 s glow time, 10 s hold time, (Ted Pella, 91000)). Purified sample was split into two conditions. IS-1 sample was made up to 100 μ M cyclothiazide (CTZ, Tocris, 07-131-0) and spun in an ultracentrifuge to pellet insoluble material prior to preparation of grids (75,000 *g*, 45 min), whereas IS-2 sample was made up to 100 μ M CTZ and 100 μ M GYKI-52466 (Tocris, 1454) prior to centrifugation (75,000 *g*, 45 min). IS-1 samples were spiked with 100 μ M GYKI-52466) and 1 mM Glu (pH 7.4) immediately before application to grids. IS-2 samples were only spiked with 1 mM Glu before application to grids. In both cases, 3 μ L of sample was applied to glow discharged grids in an FEI Vitrobot Mark IV (Thermo Fisher Scientific, wait time 10 s, blot force 5, blot time 4 s) at 8 °C and 100% humidity and plunge-frozen in liquid ethane. Grids were imaged with a 300-kV Titan Krios 3i microscope equipped with fringe free imaging, Falcon 4i camera, and Selectris energy filter set to 10 eV slit width. Micrographs were collected with a dose rate of 8.15 $e^- \text{ pixel}^{-1} \text{ s}^{-1}$ and a total dose of 40.00 $e^- \text{ \AA}^{-2}$. We collected 8,800 micrographs of the GYKI-1 condition (0.93 \AA /pix) and 7,900 micrographs of the GYKI-2 condition (0.93 \AA /pix). Automated collection was achieved with EPU software from ThermoFisher.

Image processing

Cryosparc⁷⁰ was used for all aspects of image processing. Refer to extended data figures 3 and 4 for details. The reconstruction quality was tested for anisotropic contribution to the Fourier shell correlation (FSC) with 3DFSC⁷¹.

Model building, refinement, and structural analysis

All molecular modeling, refinement, and analysis were performed with a combination of ChimeraX⁷², Isolde⁷³, Coot⁷⁴, and Phenix^{75,76} made accessible through the SBgrid consortium⁷⁷. As a starting model, the activate state GluA2-TARPy2^{15,68} (PDB 5weo) was used. Each domain (ATD, LBD, and TMD) was isolated and rigid body fit into the IS-1 full-length cryo-EM reconstruction using ChimeraX. The rigid body position of each protomer was refined by isolating them within domain and rigid body fitting. Following, each domain was joined into a single model. The exact positioning of each amino acid was fine-tuned based on the locally refined map of each domain using Coot. Then, Isolde was used to refine the model, and GYKI-52466 was placed in the map with Coot and merged into the model. Phenix was used to refine the final model. To model IS-2, the IS-1 model was rigid body fit into the IS-2 reconstruction and refined with Isolde and Phenix. Model quality was assessed with MolProbity⁷⁸. Visualizations and domain measurements were performed in ChimeraX. Pore measurements were made with MOLE Online⁷⁹.

Labeling, acquisition, and analysis for Single-Molecule FRET

HEK-293 cells overexpressing GluA2 or GluA2-TARPy2 receptors were labeled with 1:4 ratio of maleimide derivatives of Alexa 555 (donor) and Alexa 647 (acceptor) fluorophores (Invitrogen) in extracellular buffer (135 mM NaCl, 3 mM KCl, 2 mM CaCl₂, 20 mM glucose, and 20 mM HEPES, pH 7.4) at room temperature for 30 minutes. Post-labeling, the cells were washed and solubilized for 1 h at 4 °C with buffer containing 1% lauryl maltose neopentyl glycol (Anatrace, Maumee, OH, USA), 2 mM cholesteryl hydrogen succinate (MP Biomedicals, Irvine, CA, USA), and ¼ protease inhibitor tablet (Pierce™) in phosphate-buffer saline. Solubilized cells were filtered from insoluble debris by ultracentrifugation at 100,000 \times *g* for 1 h at 4 °C using a TLA 100.3 rotor.

1
2 For the slide preparation, we followed established experimental methods as previously
3 described^{80–84}. The coverslips were initially cleaned by bath sonication in Liquinox phosphate-free
4 detergent (Fisher Scientific) and acetone treatment. Further cleaning involved incubating the
5 slides in a 4.3% NH₄OH and 4.3% H₂O₂ solution at 70 °C, followed by plasma cleaning using a
6 Harrick Plasma PDC-32G Plasma Cleaner. The cleaned glass was aminosilanated using
7 Vectabond reagent (Vector Laboratories), followed by polyethylene-glycol (PEG) treatment with
8 0.25% w/w 5 kDa biotin-terminated PEG (NOF Corp., Tokyo, Japan) and 25% w/w 5 kDa mPEG
9 succinimidyl carbonate (Laysan Bio Inc., Arab, AL), then followed by a secondary PEG treatment
10 with 25 mM short-chain 333 Da MS(PEG)₄ Methyl-PEG-NHS-Ester Reagent (Thermo Scientific).
11 A microfluidics chamber was constructed on the slide, comprising an input port, a sample
12 chamber, and an output port. To coat the biotinylated surface with streptavidin molecules, 0.2
13 mg/mL Streptavidin in 1X smFRET imaging buffer (1 mM DDM (n-dodecyl-β-d-maltoside), 0.2
14 mM CHS (cholesteryl hydrogen succinate), and 1X phosphate-buffer saline was introduced into
15 the chamber and incubated for 10 min before washing with 1X phosphate-buffer saline. 60μl of
16 biotinylated Goat Anti-Mouse IgG (H + L) secondary antibody at 2.7ng/μl (Jackson
17 Immunoresearch Laboratories, Inc., West Grove, PA, USA, catalog number 115-065-003) in 1X
18 phosphate-buffer saline was then flowed through the chamber and incubated for 20 min, followed
19 by 1x phosphate-buffer saline wash.

20
21 Following this, either 60μl of anti-GluR2 at 3ng/μl for GluA2-FRET purification, Clone:
22 L21/32(BioLegend®) or 60μl of anti-TARPy2 at 2.4ng/μl for GluA2-γ2-FRET purification, Clone:
23 N245/36 (Millipore) in 1x phosphate-buffer saline was applied twice through the chamber and
24 incubated for 20 min, followed by washing with 1x phosphate-buffer saline. Bovine serum albumin
25 (0.1 mg/mL) was introduced into the chamber and incubated for 15 min, followed by 1x phosphate-
26 buffer saline wash. Detergent-solubilized purified proteins were attached to the glass slide using
27 an in situ immuno-precipitation method by applying 50 μL of sample three times through the
28 chamber and incubating for 20 min. 90 μL of oxygen-scavenging solution buffer system (ROXS)
29 was applied inside the chamber containing 1 mM methyl viologen, 1 mM ascorbic acid, 0.01%
30 w/w pyranose oxidase, 0.001% w/v catalase, 3.3% w/w glucose (all from Sigma-Aldrich, Inc., St.
31 Louis, MO, USA), 1 mM DDM (Chem-Impex, Wood Dale, IL, USA), and 0.2 mM CHS (MP
32 Biomedicals, LLC, Santa Ana, CA, USA) in phosphate-buffer saline, pH 7.4. For CTZ condition,
33 1mM glutamate, and 100 μM of CTZ were introduced into the ROXS. In the GYKI-52466 treated
34 condition, 1mM glutamate and 100 μM GYKI-52466 (MilliporeSigma, Burlington, MA, USA), were
35 introduced into the ROXS.

36
37 The smFRET data was collected using a MicroTime 200 Fluorescence Lifetime Microscope from
38 PicoQuant. A donor excitation laser (532 nm; LDH-D-TA-530; Picoquant, Berlin, Germany) and
39 an acceptor excitation laser (637 nm; LDH-D-C-640; Picoquant) were employed, utilizing a Pulsed
40 Interleaved Excitation (PIE) scheme to excite the fluorophores. Emitted photons were collected
41 through the objective lens (100X 1.4 numerical aperture; Olympus). Emission filters for the donor
42 (550 nm; FF01-582/64; AHF, Tübingen-Pfrondorf, Germany or Semrock, Rochester, NY) and
43 acceptor (650 nm 2XH690/70; AHF) were used to select photons for each detection channel.
44 These photons were directed to two SPAD photodiodes (SPCM CD3516H, Excelitas
45 technologies, Waltham, MA) to measure the fluorescence intensity for each fluorophore. The
46 donor and acceptor fluorescence intensities were recorded for one protein at a time.

47
48 In our data analysis, we selected only those molecules that exhibited a single photobleaching
49 step in both the donor and acceptor channels. This stringent criterion ensured that only one donor
50 and one acceptor fluorophore were attached to each GluA2 protein. Furthermore, we retained
51 only those molecules that displayed anti-correlation between the donor and acceptor

1 fluorescence, confirming that the fluorophores were engaged in FRET prior to photobleaching.
2 Molecules not exhibiting these characteristics were excluded from the final analysis. The number
3 of molecules included in the analysis for each condition is as follows: GluA2- γ 2-FRET (CTZ = 76,
4 GYKI-52466 = 77), GluA2-FRET (CTZ = 62*, GYKI-52466 = 96). *30 molecules with 1mM of
5 glutamate and 100 μ M CTZ were obtained from Carrillo and Shaikh et al. (2020)³³.
6

7 The corrected donor and acceptor intensities over time were then used to calculate a FRET
8 efficiency trace for each molecule. These traces were pooled for each condition and used to
9 create FRET efficiency distribution histograms for each condition. We conducted Step Transition
10 and State Identification (STaSI) analysis to determine the number of conformational states in each
11 condition⁸⁵. The smallest number of states that accurately described the data as determined by
12 the STaSI analysis was adopted as the final number of states for each condition. Using the results
13 of the STaSI analysis and Origin software (OriginLab), the FRET efficiency histograms for each
14 condition were fitted with Gaussian curves to represent the conformational states within the
15 overall distributions.
16

17 To test for the statistical difference between conditions CTZ and GYKI, FRET efficiency mode
18 was obtained for each day as this more accurately represents the histogram peak. The mean and
19 standard deviation were calculated across these days. A two-sample t-test, assuming a one-tail
20 distribution with known variances, was used to assess the statistical differences between the
21 conditions using Origin software (OriginLab).
22

23 *Electrophysiology*

24

25 For electrophysiological measurements of GluA2-TARPy2, 1 μ g of DNA was transfected in 3cm
26 culture dishes using Lipofectamine 2000. Patch-clamp recordings were performed 24–48 h after
27 transfection using fire-polished borosilicate glass (Sutter instruments, Novato, CA, USA) pipettes
28 with 1–4 megaohms resistance were filled with internal solution: 110 mM CsF, 30 mM CsCl, 4
29 mM NaCl, 0.5 mM CaCl₂, 10 mM HEPES, and 5 mM EGTA (adjusted to pH 7.4 with CsOH). The
30 extracellular solution consisted of 150 mM NaCl 3 mM KCl, 2 mM CaCl₂, and 10 mM HEPES
31 adjusted to pH 7.4 with NaOH. External solutions were locally applied to lifted cells or patches
32 using a SF-77B perfusion fast-step (Warner Instruments, Holliston, MA, USA). For inhibition-dose
33 response, 1 mM of glutamate and 100 μ M CTZ was applied first to obtain control condition
34 followed by 2-3 different concentrations of GYKI with 1 mM of glutamate. For each GYKI
35 concentration, the same GYKI concentration was preincubated in extracellular buffer. Recordings
36 were performed using an Axopatch 200B amplifier (Molecular Devices, San Jose, CA, USA) at
37 -60 mV hold potential, acquired at 2kHz using pCLAMP10 software (Molecular Devices, Axon
38 200B and Digidata 1550A; Molecular Devices). Individual patch-clamp traces were analyzed, and
39 data was reduced to 300 μ s sampling using Clampfit 11 software (Molecular Devices, San Jose,
40 CA, USA). IC₅₀ was quantified from the average residual current using Clampfit 11.
41 Representative traces graphed, normalized, and calculated using Origin software (OriginLab).
42

43 *Free Energy Molecular Dynamics Simulations*

44

45 The conformational free energy landscape, or potential of mean force (PMF), of the LBD dimer
46 was computed using umbrella sampling simulations. A two-dimensional order parameter (χ_1 , χ_2)
47 describes large-scale conformational transitions between each LBD of the dimer. χ_1 and χ_2 each
48 indicates the distance between the center of mass (COM) of the atoms N, CA, CB, C, and O in
49 residues 482–488, helix D, and the COM of the same atoms in residues 748–757, helix J.
50 Helices D and J form the dimer interface. Coordinates for the umbrella sampling windows were
51 generated via targeted (biased-potential) molecular dynamics (MD) simulations using

1 CHARMM⁸⁶ in 1 Å increments along χ_1 and χ_2 . These coordinates were initiated from the crystal
2 structure of a glutamate-bound GluA2 LBD dimer (PDB ID 1FTJ)⁴⁵. For GluA2-L483Y, these
3 coordinates were initiated from the crystal structure of the mutant LBD dimer (PDB: 1LB8)²².
4 Missing residues were built using the ModLoop server⁸⁷, and missing residue side chains were
5 built using SCWRL4⁸⁸.

6
7 All simulations were performed using CHARMM36 with explicit solvent at 300 K. The all-atom
8 potential-energy function PARAM27 for proteins^{89,90} and the TIP3P potential-energy function for
9 water⁹¹ were used. Each simulation system contains ~56,000 atoms, and 39 Na⁺ and 47 Cl⁻
10 ions were added in the bulk solution to give ~150 mM NaCl and an electrically neutral system.
11 Periodic boundary conditions were used with an orthorhombic cell with approximate dimensions
12 96 Å x 78 Å x 78 Å. Equilibration was carried out in the NVT ensemble with restraints applied to
13 the backbone and sidechain atoms, which were slowly released over the course of the
14 equilibration. Production simulations were carried out in the NPT ensemble at 1 atm and 300
15 K⁹². Long-range electrostatic interactions were computed using the particle mesh Ewald (PME)
16 algorithm⁹³.

17
18 The PMF comprises 140 umbrella sampling windows totaling 364 ns of simulation time and 398
19 ns for GluA2-L483Y. Harmonic biasing potentials with a force constant of 2 kcal mol⁻¹ Å⁻²
20 centered on (χ_1 , χ_2) were used. Each PMF was computed using the weighted histogram
21 analysis method (WHAM)^{94,95} to unbias and recombine the sampled distribution functions from
22 all windows.

23 **Conflict of Interest**

24
25
26 R. L. H. is scientific cofounder and Scientific Advisory Board (SAB) member of Neumora
27 Therapeutics and SAB member of MAZE Therapeutics.

28 **Data Availability**

29
30
31 All cryo-EM reconstructions will be deposited into the Electron Microscopy Data Bank (EMDB)
32 upon publication. All micrographs from the IS-1 and IS-2 datasets will be deposited into the
33 Electron Microscopy Public Image Archive (EMPIAR) upon publication. All structural models
34 generated from cryo-EM will be deposited in the Protein Data Bank upon publication. All
35 conformers from MD simulation trajectories, data from umbrella sampling, analysis code, will be
36 publicly available from Zenodo upon publication of this work.

37 **Acknowledgements**

38
39
40 We thank members of the Twomey, Haganir, Lau, and Jayaraman labs for insightful discussions
41 and L. Dillard (Twomey lab) for assistance in collecting the IS-2 dataset. We thank M. Catipovic
42 (JHU) for insightful comments on the manuscript. All cryo-EM data was collected at the Beckman
43 Center for Cryo-EM at Johns Hopkins with assistance from D. Sousa and D. Ding. Computational
44 resources were provided by the Maryland Advanced Research Computing Center (MARCC) and
45 Advanced Research Computing at Hopkins (ARCH) at Johns Hopkins University.

46 **Funding**

47
48
49 E.C.T is supported by the Searle Scholars Program (Kinship Foundation #22098168) and the
50 Diana Helis Henry Medical Research Foundation (#142548). R.L.H. is supported by National
51 Institutes of Health (NIH) grants R01 NS036715 and R01 MH112152. A.Y.L is supported by NIH

1 grant R01 GM094495. V.J. is supported by NIH grant R35 GM122528. C.U.G. is supported by
2 NIH grant F99NS130928. W.D.H. is supported by NIH grant K99 MH132811.

3

4 **Author Contributions**

5

6 E.C.T. and R.L.H. supervised all aspects and planning of this research. E.C.T. and W.D.H.
7 designed the project. E.C.T. and W.D.H. wrote the manuscript with input from all authors. W.D.H.
8 prepared samples for cryo-EM, collected cryo-EM data, processed cryo-EM data, analyzed data,
9 and built models with E.C.T. A.M.R. assisted with protein expression, model building, data
10 analysis, structural analysis, and in uncovering the inhibition mechanism with W.D.H. V.J., C.U.G.
11 designed the smFRET and electrophysiology experiments with input from E.C.T. and W.D.H.
12 C.U.G. carried out the smFRET and electrophysiology experiments under the supervision of V.J.
13 C.U.G. carried out statistical analysis of smFRET and electrophysiology data under supervision
14 of V.J. A.Y.L. planned and carried out all molecular dynamics simulation studies and analysis.

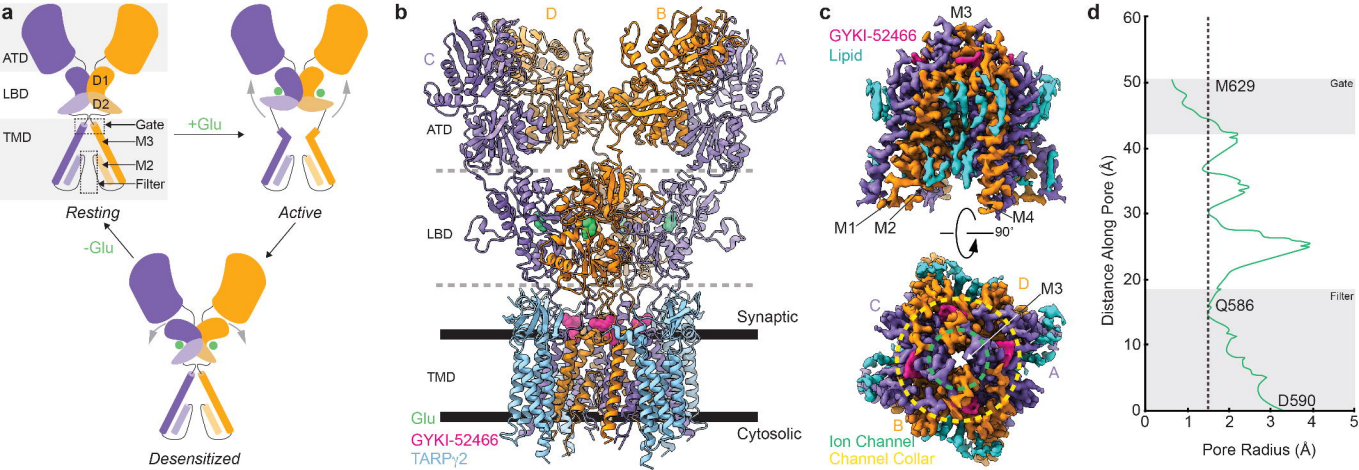
15

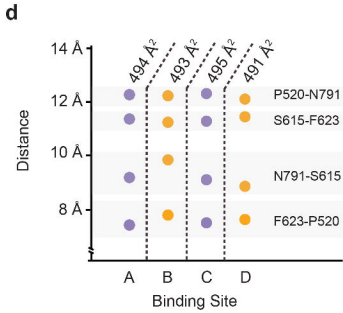
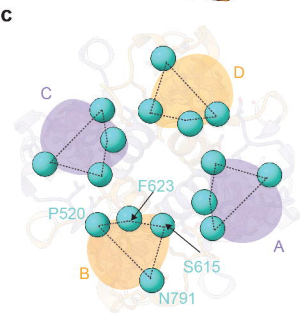
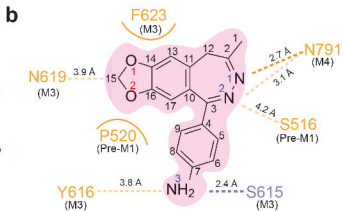
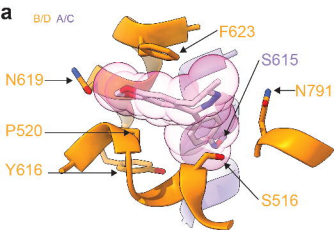
1 Cryo-EM data collection, refinement, and validation statistics

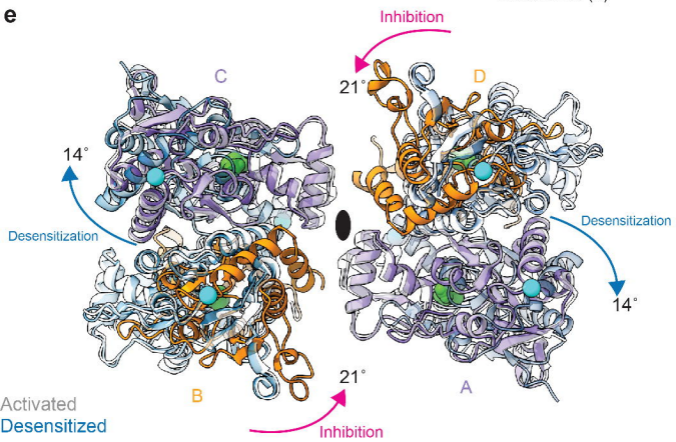
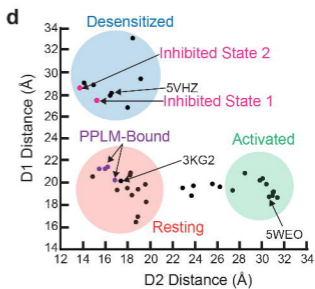
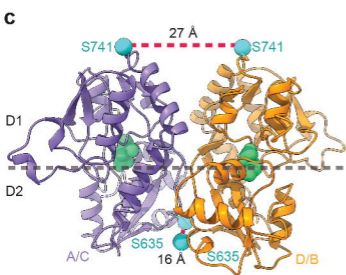
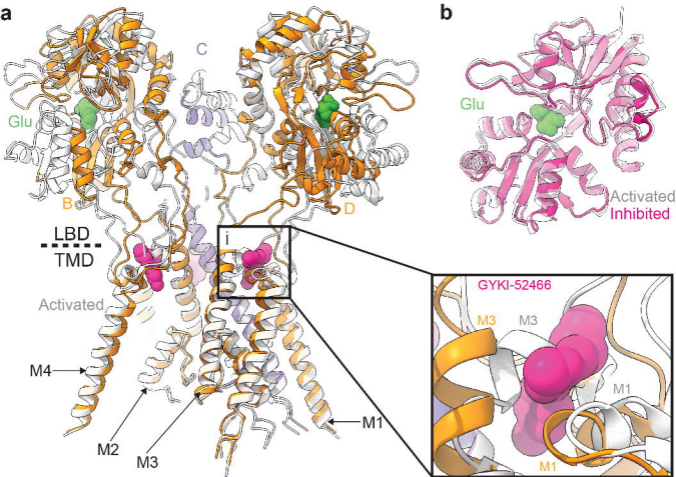
2

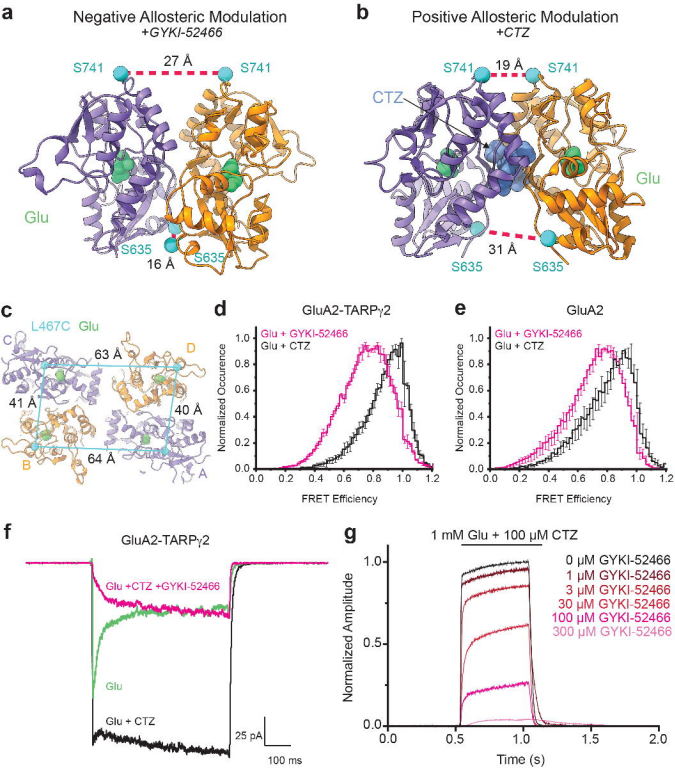
	IS-1 (EMDB-xxxx) (PDB xxxx)	IS-2 (EMDB-xxxx) (PDB xxxx)
Data collection and processing		
Magnification	130,000x	130,000x
Voltage (kV)	300	300
Electron exposure (e ⁻ /Å ²)	40	40
Defocus range (μm)	-1.0 – 2.6	-1.0 – 2.6
Pixel size (Å)	0.93	0.93
Symmetry imposed	C2	C2
Initial particle images (no.)	1,258,087	1,031,751
Final particle images (no.)	123,729	130,474
Map resolution (Å)		
FSC = 0.143		
Map resolution range (Å)	2 – 13	2.5 – 13
Refinement		
Initial model used (PDB code)	5WEO	This study, IS-1
Model resolution (Å)	4.2	3.55
FSC = 0.143		
Model resolution range (Å)	3.4 – 4.1	3.2 – 4.1
Map sharpening <i>B</i> factor (Å ²)	-65	-120
Model composition		
Non-hydrogen atoms	25180	25180
Protein residues	3186	3186
Ligands	4	4
<i>B</i> factors (Å ²)		
Protein	0.48/164.05/76.91	0/391.17/121.95
Ligand	12.19/43.65/29.89	0.01/9.83/4.8
R.m.s. deviations		
Bond lengths (Å)	0.003	0.004
Bond angles (°)	0.641	0.651
Validation		
MolProbity score	1.7	1.66
Clashscore	6.58	7.04
Poor rotamers (%)	1.33	0.34
Ramachandran plot		
Favored (%)	96.3	96.05
Allowed (%)	3.51	3.77
Disallowed (%)	0.19	0.18

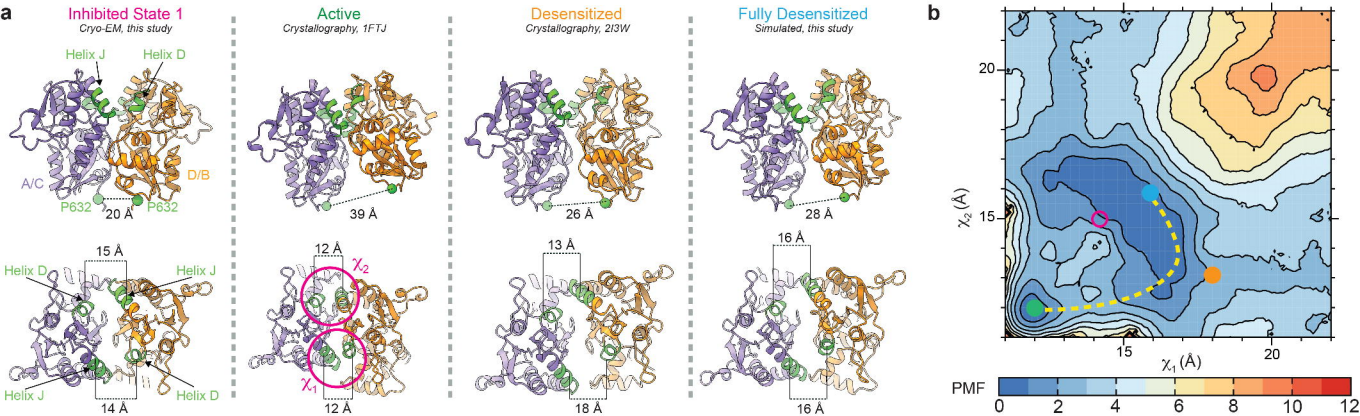
3

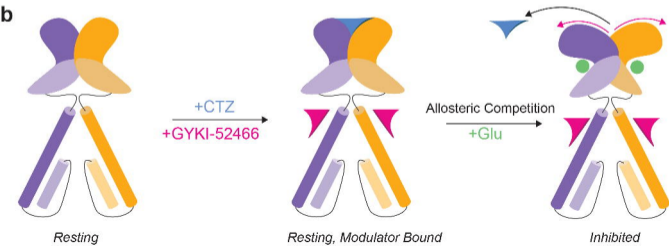
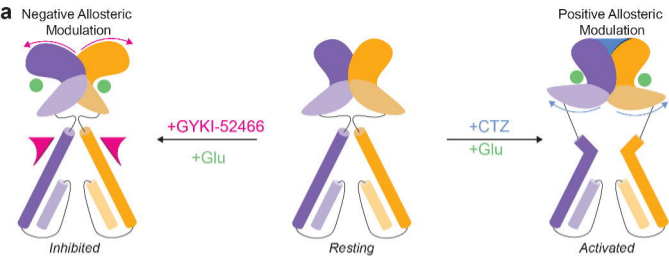


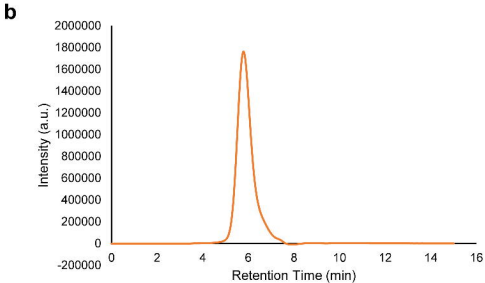
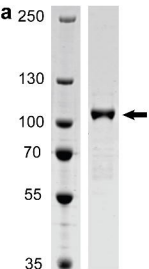










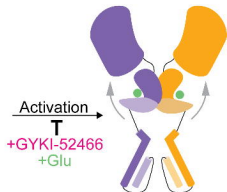
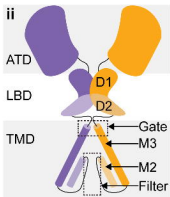


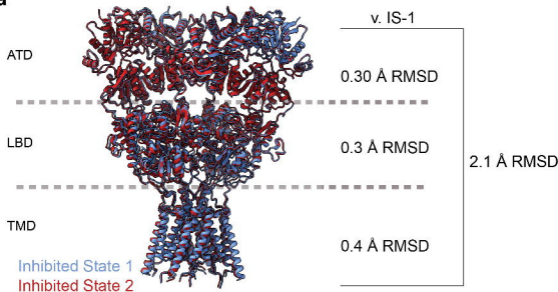
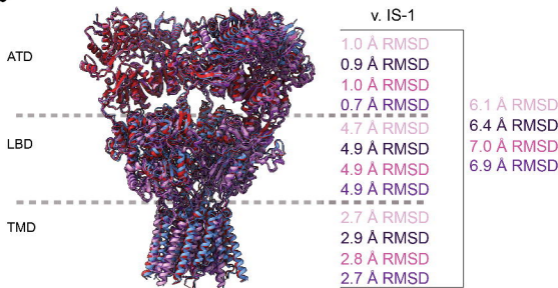
c

i

IS-1: Pre-Incubation (CTZ)
+ Spike (Glu & GYKI-52466)

IS-2: Pre-Incubation (CTZ & GYKI-52466)
+ Spike (Glu)



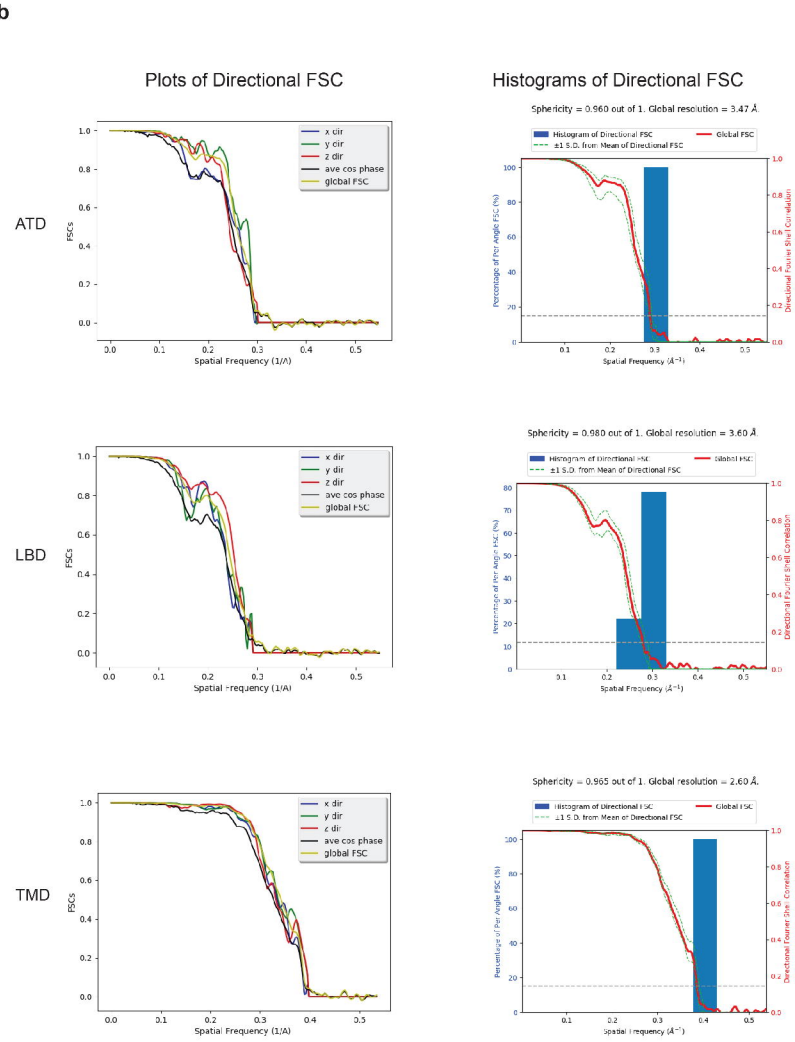
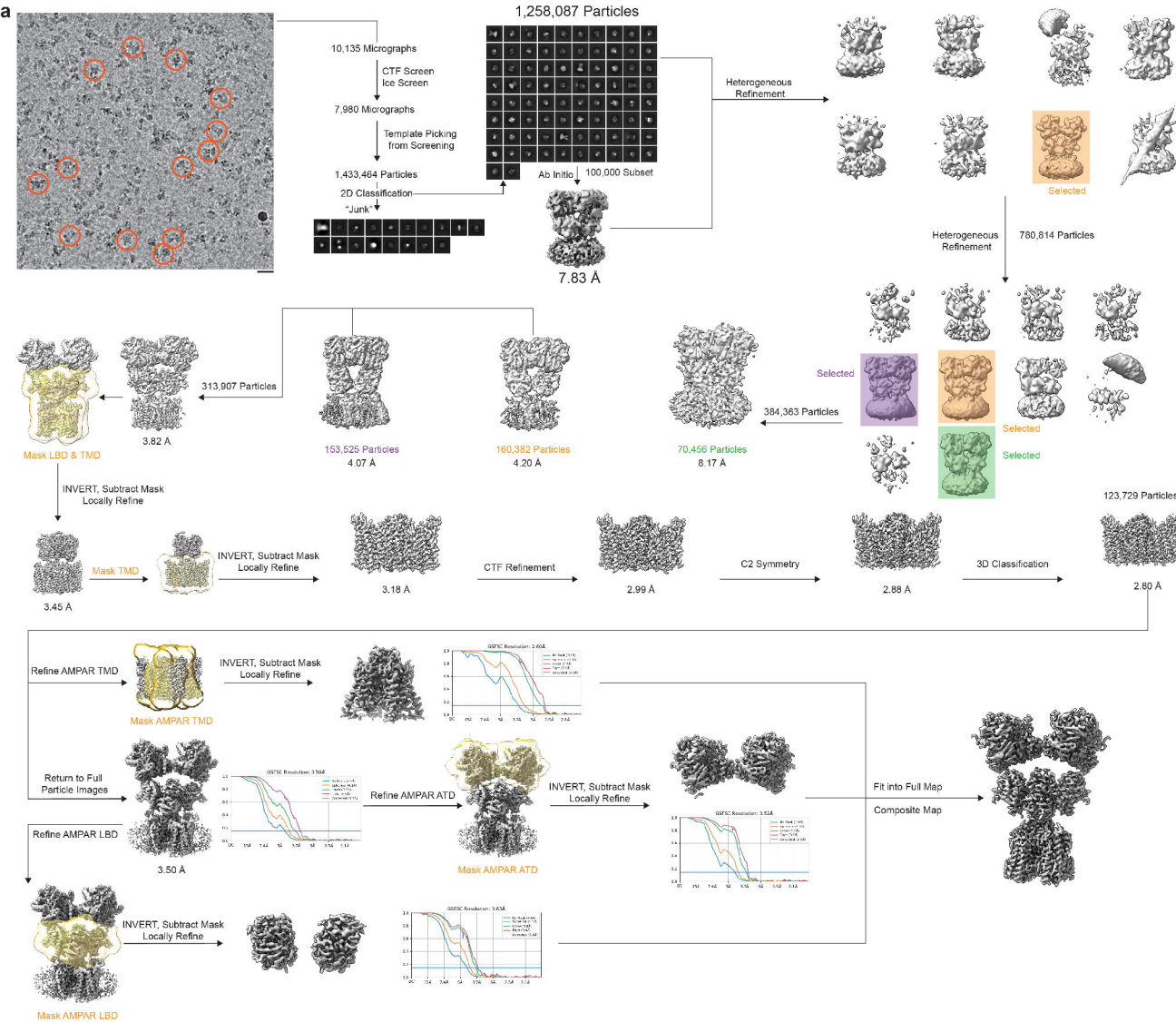
a**b**

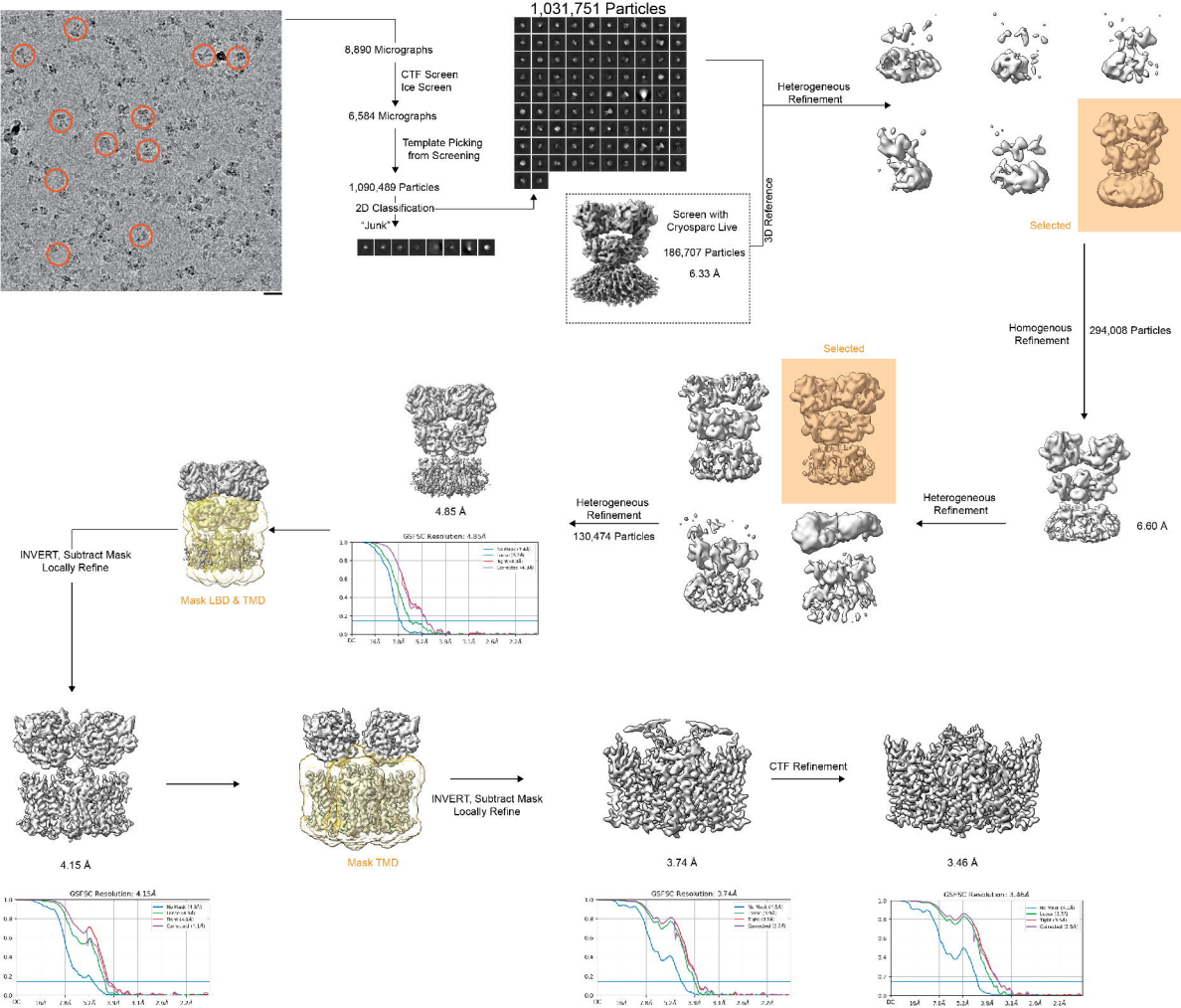
Apo +CP465022 (5L1E)

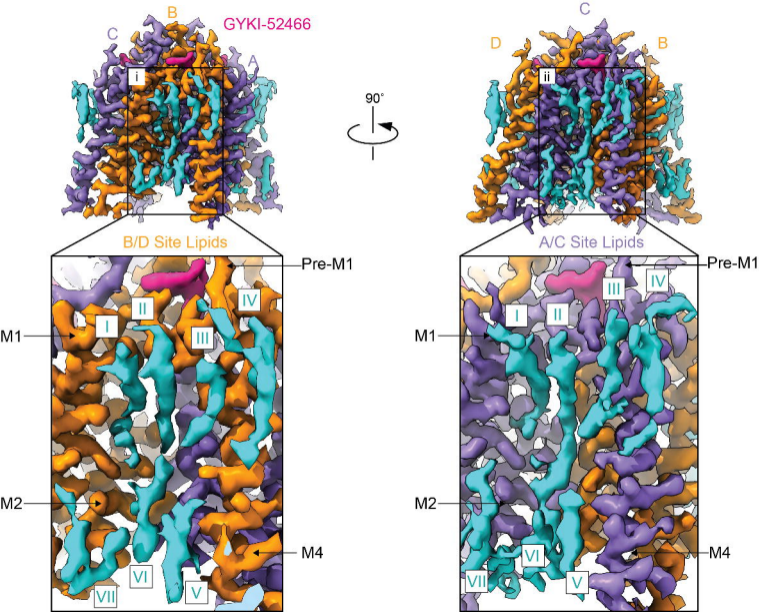
Apo +Perampanel (5L1F)

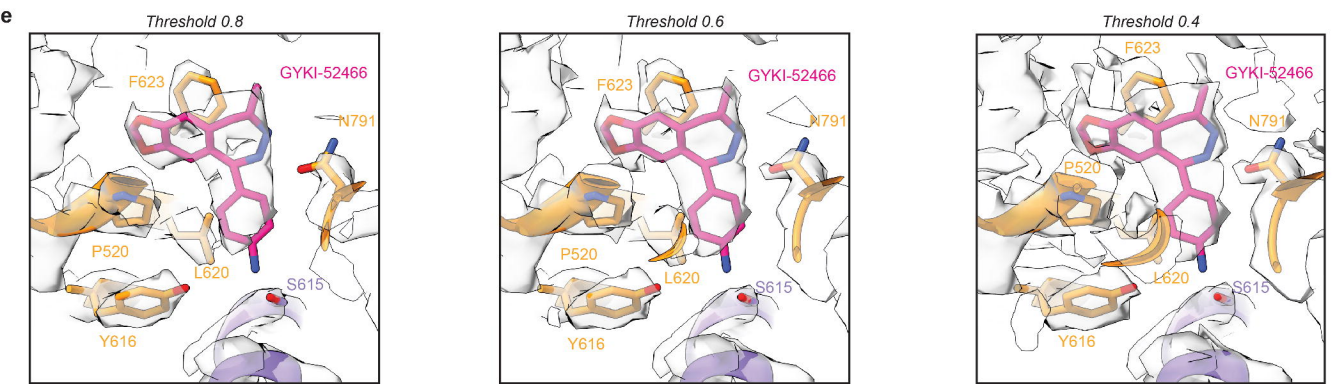
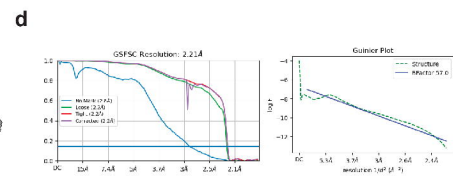
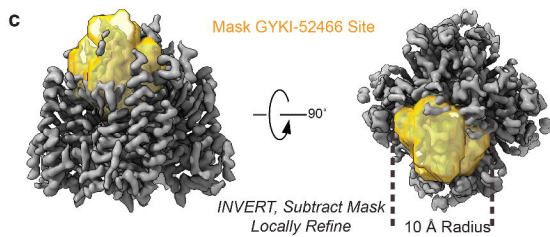
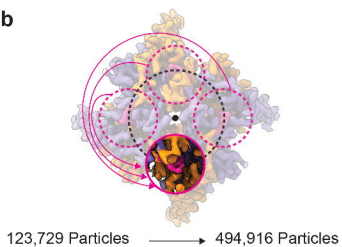
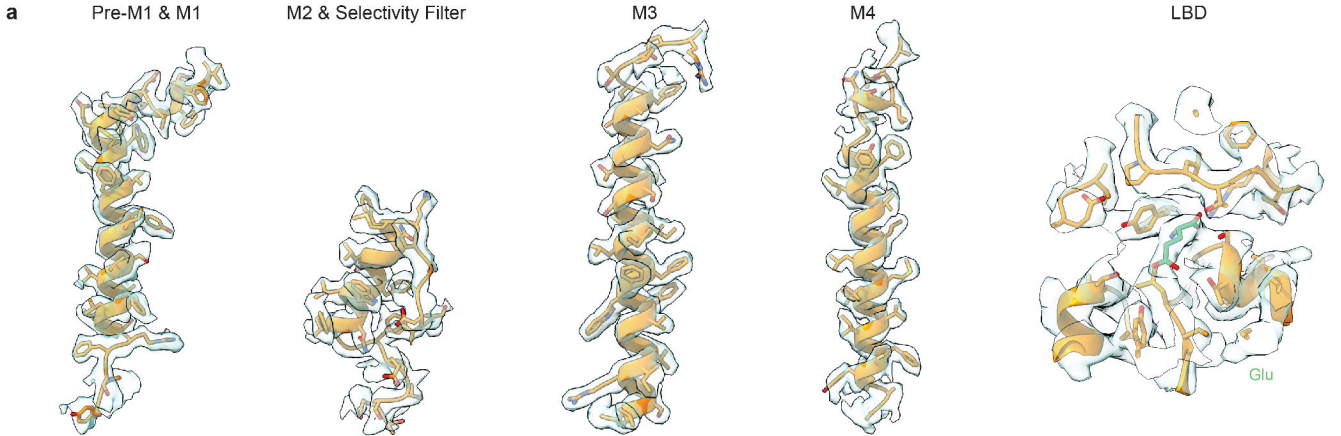
Apo +GYKI-Br (5L1G)

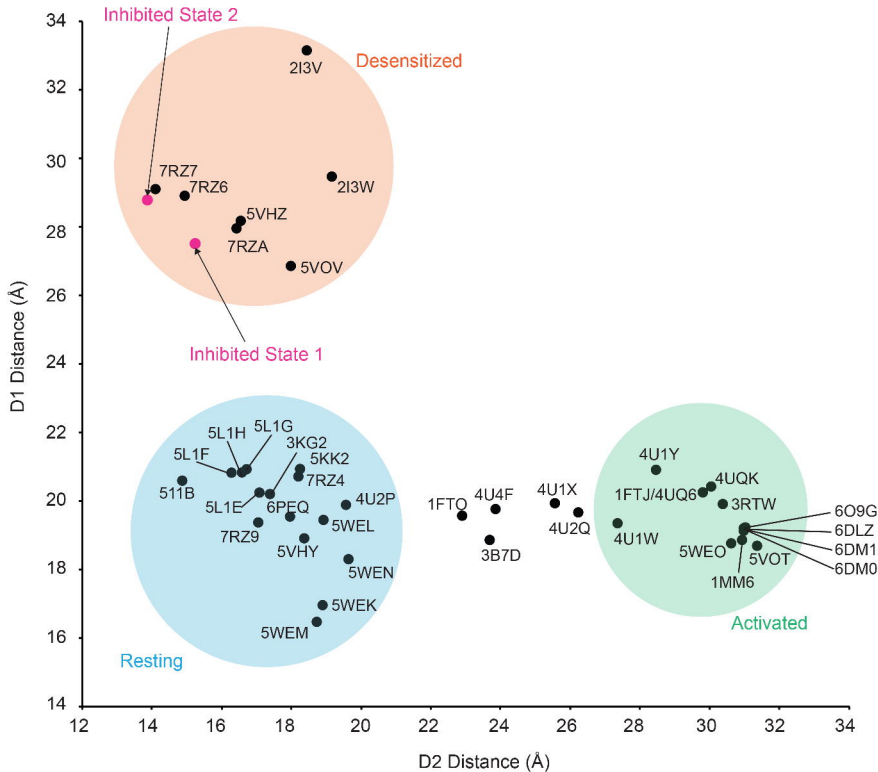
Apo +GYKI-53655 (5L1H)

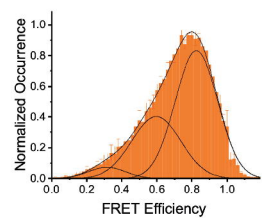
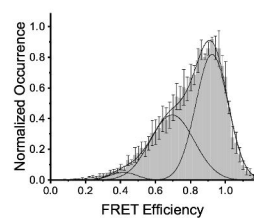
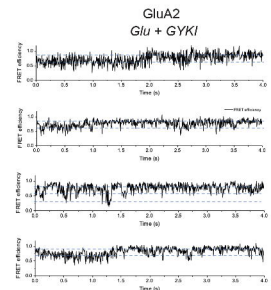
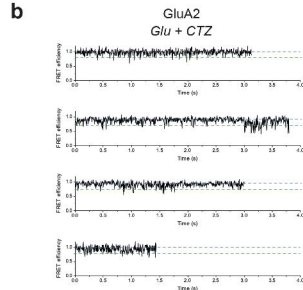
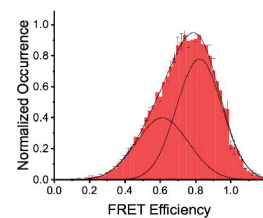
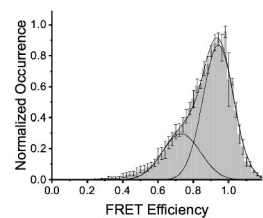
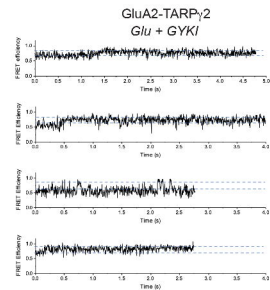
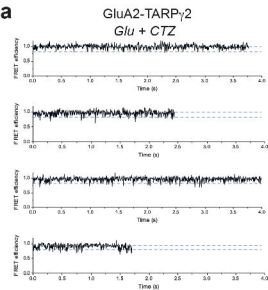












c

Construct	Condition	N	Mean	SE	p value
GluA2- γ 2-FRET	CTZ	3	0.973	0.0067	0.00114
	GYKI	3	0.767	0.029	
GluA2-FRET	CTZ	3*	0.920	0.031	0.00552
	GYKI	5	0.804	0.017	

